

Six Months of Multi-Wavelength Follow-up of the Tidal Disruption Candidate ASASSN-14li and Implied TDE Rates from ASAS-SN

T. W.-S. Holoien^{1,2,3*}, C. S. Kochanek^{1,2}, J. L. Prieto^{4,5}, K. Z. Stanek^{1,2}, Subo Dong⁶, B. J. Shappee^{7,8,9}, D. Grupe¹⁰, J. S. Brown¹, U. Basu^{1,11}, J. F. Beacom^{1,2,12}, D. Bersier¹³, J. Brimacombe¹⁴, A. B. Danilet¹², E. Falco¹⁵, Z. Guo⁶, J. Jose⁶, G. J. Herczeg⁶, F. Long⁶, G. Pojmanski¹⁶, G. V. Simonian¹, D. M. Szczygieł¹⁶, T. A. Thompson^{1,2}, J. R. Thorstensen¹⁷, R. M. Wagner^{1,18}, and P. R. Woźniak¹⁹

¹ Department of Astronomy, The Ohio State University, 140 West 18th Avenue, Columbus, OH 43210, USA

² Center for Cosmology and AstroParticle Physics (CCAPP), The Ohio State University, 191 W. Woodruff Ave., Columbus, OH 43210, USA

³ US Department of Energy Computational Science Graduate Fellow

⁴ Núcleo de Astronomía de la Facultad de Ingeniería, Universidad Diego Portales, Av. Ejército 441, Santiago, Chile

⁵ Millennium Institute of Astrophysics, Santiago, Chile

⁶ Kavli Institute for Astronomy and Astrophysics, Peking University, Yi He Yuan Road 5, Hai Dan District, Beijing, China

⁷ Carnegie Observatories, 813 Santa Barbara Street, Pasadena, CA 91101, USA

⁸ Hubble Fellow

⁹ Carnegie-Princeton Fellow

¹⁰ Department of Earth and Space Science, Morehead State University, 235 Martindale Dr., Morehead, KY 40351, USA

¹¹ Grove City High School, 4665 Hoover Road, Grove City, OH 43123, USA

¹² Department of Physics, The Ohio State University, 191 W. Woodruff Ave., Columbus, OH 43210, USA

¹³ Astrophysics Research Institute, Liverpool John Moores University, 146 Brownlow Hill, Liverpool L3 5RF, UK

¹⁴ Coral Towers Observatory, Cairns, Queensland 4870, Australia

¹⁵ Whipple Observatory, Smithsonian Institution, 670 Mt. Hopkins Road, P. O. Box 6369, Amado, AZ 85645m USA

¹⁶ Warsaw University Astronomical Observatory, Al. Ujazdowskie 4, 00-478 Warsaw, Poland

¹⁷ Department of Physics and Astronomy, Dartmouth College, Hanover, NH 03755, USA

¹⁸ LBT Observatory, University of Arizona, Tucson, AZ 85721-0065

¹⁹ Los Alamos National Laboratory, Mail Stop B244, Los Alamos, NM 87545, USA

6 February 2022

ABSTRACT

We present ground-based and *Swift* photometric and spectroscopic observations of the candidate tidal disruption event (TDE) ASASSN-14li, found at the center of PGC 043234 ($d \simeq 90$ Mpc) by the All-Sky Automated Survey for SuperNovae (ASAS-SN). The source had a peak bolometric luminosity of $L \simeq 10^{44}$ ergs s⁻¹ and a total integrated energy of $E \simeq 7 \times 10^{50}$ ergs radiated over the ~ 6 months of observations presented. The UV/optical emission of the source is well-fit by a blackbody with roughly constant temperature of $T \sim 35,000$ K, while the luminosity declines by roughly a factor of 16 over this time. The optical/UV luminosity decline is broadly consistent with an exponential decline, $L \propto e^{-t/t_0}$, with $t_0 \simeq 60$ days. ASASSN-14li also exhibits soft X-ray emission comparable in luminosity to the optical and UV emission but declining at a slower rate, and the X-ray emission now dominates. Spectra of the source show broad Balmer and helium lines in emission as well as strong blue continuum emission at all epochs. We use the discoveries of ASASSN-14li and ASASSN-14ae to estimate the TDE rate implied by ASAS-SN, finding an average rate of $r \simeq 4.1 \times 10^{-5}$ yr⁻¹ per galaxy with a 90% confidence interval of $(2.2 - 17.0) \times 10^{-5}$ yr⁻¹ per galaxy. ASAS-SN found roughly 1 TDE for every 70 Type Ia supernovae in 2014, a rate that is much higher than that of other surveys.

Key words: accretion, accretion disks — black hole physics — galaxies: nuclei

1 INTRODUCTION

A star orbiting a supermassive black hole (SMBH) can be torn apart if its orbit brings it within the tidal disruption radius of the SMBH where tidal shear forces overpower the self-gravity of the star. In these so-called “tidal disruption events” (TDEs), roughly half of the mass of the star may be ejected while the rest of the stellar material is accreted onto the black hole, resulting in a short-lived ($t \lesssim 1$ yr) accretion flare (e.g., Lacy, Townes & Hollenbach 1982; Rees 1988; Phinney 1989; Evans & Kochanek 1989). In cases where the central black hole has a mass $M_{BH} \lesssim 10^7 M_{\odot}$, the initial fallback rate is super-Eddington, and the eventual rate at which material returns to pericenter roughly follows a $t^{-5/3}$ power law (Evans & Kochanek 1989; Phinney 1989). It is commonly assumed that the resulting luminosity of the TDE flare will be proportional to the rate of return of the stellar material to pericenter, but the exact return rates depend on the complex physics associated with the evolution of the accretion stream (e.g., Kochanek 1994; Lodato & Rossi 2011; Guillochon & Ramirez-Ruiz 2015; Shiokawa et al. 2015).

While the accretion of the stellar material powers the TDE flare, direct emission from the disk is only expected to be seen in late phases, with the emission for the majority of the duration of the flare likely dominated by a photosphere formed in the stellar debris (Evans & Kochanek 1989; Loeb & Ulmer 1997; Ulmer 1999; Strubbe & Quataert 2009). However, simulations have shown that the source of emission seen by the observer likely depends on the viewing angle of the event (Guillochon, Manukian & Ramirez-Ruiz 2014). While sharing some characteristics similar to both supernovae (SNe) and active galactic nuclei (AGN), TDEs are expected to show unique spectral characteristics and light curve evolution that would distinguish them from such transients. Notably, Holoien et al. (2014a) showed that TDEs exhibit significant long-lasting blue–ultraviolet (UV) flux increases compared to supernovae and Arcavi et al. (2014) found that TDE candidates span a range of H- to He-dominated spectral features. As the light emitted during the TDE may be sensitive to the black hole spin and mass (e.g., Magorrian & Tremaine 1999; Ulmer 1999; Graham et al. 2001; Metzger & Stone 2015), the detection and study of TDEs may provide a unique method for studying the properties of SMBHs.

A number of candidate TDEs were discovered by UV and X-ray surveys (e.g., NGC5905; Komossa & Greiner (1999), RX J1624+75; Grupe, Thomas & Leighly (1999), A1795; Donato et al. (2014), Swift J164449.3+573451; Burrows et al. (2011); Bloom et al. (2011); Levan et al. (2011); Zauderer et al. (2011), Swift J0258.4+0516; Cenko et al. (2012b), and GALEX candidates D1-9, D3-13, and D23H-1; Gezari et al. (2008, 2009)). Many of these cases did not show correspondingly strong optical emission, and in some cases they were discovered in sparse archival data, limiting their usefulness as probes of TDE physics. In recent years, however, a number of candidates have been found by high-cadence optical surveys, including the All-Sky Automated Survey for Supernovae (ASASSN-14ae, Holoien et al. 2014a), the Palomar Transient Factory (PTF10iya, Cenko et al. 2012a; PTF09ge, PTF09axc, and PTF09djl, Arcavi et al. 2014), Pan-STARRS (PS1-10jh, Gezari et al. 2012; PS1-11af, Chornock et al. 2014), and the Sloan Digital

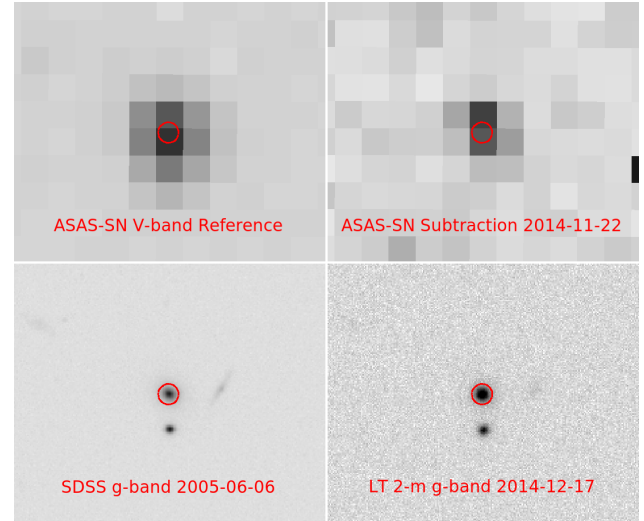


Figure 1. Discovery images of ASASSN-14li. The top-left panel shows the ASASSN V-band reference image and the top-right panel shows the ASASSN subtracted image from 2014 November 22, the date of discovery. The bottom-left panel shows the archival SDSS *g*-band image of the host galaxy PGC 043234 and the right panel shows an LT 2-m *g*-band image taken during our follow-up campaign. The dates of the observations are listed on each panel. The red circles have radii of $3''.0$ and are centered on the position of the transient measured in the LT image.

Sky Survey (TDE 1 and TDE 2, van Velzen et al. 2011). These transients typically showed strong UV and optical emission but no associated X-ray emission, and were often better-studied than previous candidates, as they were discovered and followed up by survey projects searching their data in real-time. Optically discovered candidates have provided new opportunities to study these rare transients in greater detail than previously possible, and recent estimates based on optical TDE discoveries put the TDE rate at $\dot{N}_{TDE} = (1.5-2.0)_{-1.3}^{+2.7} \times 10^{-5} \text{ yr}^{-1}$ per galaxy (van Velzen & Farrar 2014). However, there is still tension between this estimate and the rates predicted by modeling two-body scattering of stars in galactic nuclei (typically $\sim 10^{-4} \text{ yr}^{-1}$ per galaxy), which may in part be due to the fact that only a small fraction of TDEs are optically luminous (Stone & Metzger 2014; Metzger & Stone 2015). Selection effects from optical surveys may also play a role in this discrepancy, and a careful determination of TDE detection efficiency and completeness is needed to determine the degree to which the actual TDE rate may be higher than the rates inferred from optical surveys.

In this manuscript we describe the discovery and follow-up observations of ASASSN-14li, a candidate TDE discovered by the All-Sky Automated Survey for SuperNovae (ASASS-SN¹; Shappee et al. 2014). ASASS-SN is a long-term project to monitor the whole sky on a rapid cadence to find nearby supernovae (e.g., Holoien et al. 2014b) and other bright transients, such as AGN activity (e.g., Shappee et al. 2014), extreme stellar flares (e.g., Schmidt et al. 2014), outbursts in young stellar objects (e.g., Holoien et al. 2014c), and cataclysmic variable stars (e.g., Kato et al.

¹ <http://www.astronomy.ohio-state.edu/~assassin/>

2013, 2014). Our transient source detection pipeline was triggered on 2014 November 22, detecting a new source with $V = 16.5 \pm 0.1$ mag (Jose et al. 2014). The object was also detected on 2014 November 11 at $V = 15.8 \pm 0.1$ mag, but is not detected ($V \gtrsim 17$ mag) in data obtained on 2014 July 13 and before. Unfortunately, no data were obtained between 2014 July 13 and 2014 November 11 as the galaxy was behind the Sun.

A search at the object’s position (J2000 RA/Dec = 12:48:15.23/+17:46:26.22) in the Sloan Digital Sky Survey Data Release 9 (SDSS DR9; Ahn et al. 2012) catalog revealed the source of the outburst to be the galaxy PGC 043234 (VII Zw 211) at redshift $z = 0.0206$, corresponding to a luminosity distance of $d = 90.3$ Mpc ($H_0 = 73$ km s $^{-1}$ Mpc $^{-1}$, $\Omega_M = 0.27$, $\Omega_\Lambda = 0.73$), and that the ASAS-SN source position was consistent with the center of the host galaxy. Follow-up images obtained on 2014 November 28 with the Las Cumbres Observatory Global Telescope Network (LCOGT) 1-m telescope at McDonald Observatory (Brown et al. 2013) and on 2014 November 30 with the *Swift* UltraViolet and Optical Telescope (UVOT; Roming et al. 2005) confirmed the detection of the transient.

In order to constrain any offset between the source of the outburst and the nucleus of the host galaxy we first astrometrically aligned an image of the transient taken with the 2-m Liverpool Telescope (LT; Steele et al. 2004) with the archival SDSS image of the host galaxy. From this aligned image, we measure an offset of 0.43 ± 0.52 pixels (0.17 ± 0.21 arcseconds, or 74.4 ± 91.9 parsecs) between the position of the brightest pixel in the host galaxy in the LT image and the position of the brightest pixel in the SDSS image. This offset is consistent with the source of the outburst being the nucleus of the host galaxy, which provides support for a TDE interpretation of the event. Figure 1 shows the ASAS-SN V -band reference image of the host galaxy and the ASAS-SN V -band subtraction image from the discovery epoch as well as archival SDSS and post-discovery LT g -band images.

The archival SDSS spectrum of PGC 043234 shows little evidence of strong AGN activity. A follow-up spectrum of the nuclear region of the host obtained on 2014 November 30 with the SuperNova Integral Field Spectrograph (SNIFS; Lantz et al. 2004) mounted on the University of Hawaii 2.2-m telescope showed a broad H α emission feature at the redshift of the host with a FWHM $\simeq 9000$ km s $^{-1}$ and increased emission at bluer wavelengths. In addition to this follow-up spectrum, follow-up photometry of the source obtained on 2014 November 30 with the *Swift* X-ray Telescope (XRT; Burrows et al. 2005) and UVOT showed strong soft X-ray emission and ultraviolet emission from a location consistent with the host nucleus. Given these observations, we determined that ASASSN-14li was a potential tidal disruption event, and began an extensive follow-up campaign in order to characterize the transient.

In §2 we describe pre-outburst data, including photometry and spectroscopy, of the host galaxy as well as new observations obtained of the transient during our follow-up campaign. In §3 we analyze these data to model the transient’s luminosity and temperature evolution and compare the properties of ASASSN-14li to those of other TDE candidates in literature. Finally, in §4, we use the TDE discoveries by ASAS-SN to estimate the rate of these transients in the nearby universe.

Table 1. Photometry of the Host Galaxy

Filter	Magnitude	Magnitude Uncertainty
<i>NUV</i>	19.77	0.06
<i>u</i>	17.61	0.03
<i>g</i>	16.15	0.03
<i>r</i>	15.63	0.03
<i>i</i>	15.37	0.03
<i>z</i>	15.17	0.03
<i>J</i>	14.30	0.07
<i>H</i>	13.48	0.07
<i>K_s</i>	13.20	0.09

These are 5 $''$ 0 radius aperture magnitudes from GALEX, SDSS, and 2MASS.

2 OBSERVATIONS AND SURVEY DATA

In this section we summarize the available archival survey data of the transient host galaxy PGC 043234 as well as our new photometric and spectroscopic observations of ASASSN-14li.

2.1 Archival Data

We retrieved archival reduced *ugriz* images of PGC 043234 from SDSS DR9 and measured the fluxes in a 5 $''$ 0 aperture radius. This aperture radius was also used to measure the source flux in follow-up data, and was chosen to match the *Swift* PSF. We also obtained near-IR *JHK_s* images from the Two-Micron All Sky Survey (2MASS; Skrutskie et al. 2006) and measured 5 $''$ 0 aperture magnitudes using the same procedure. Finally, we obtained a near-UV image of the host galaxy from the Galaxy Evolution Explorer (GALEX) Data Release 7 and measured the magnitude of the host using PSF photometry. The measured fluxes from GALEX, SDSS, and 2MASS were then used for host galaxy SED modeling and for subtracting the host galaxy flux from follow-up data containing the transient. We present the measured 5 $''$ 0 aperture magnitudes from the SDSS and 2MASS images and the PSF magnitude from the GALEX image in Table 1.

There are no archival Spitzer, Herschel, Hubble Space Telescope (HST), Chandra, or X-ray Multi-Mirror Mission (XMM-Newton) observations of PGC 043234. Examining data from the ROSAT All-Sky Survey, we do not detect the host galaxy with a 3-sigma upper limit of 1.8×10^{-2} counts s $^{-1}$, corresponding to 7.5×10^{-14} ergs s $^{-1}$ cm $^{-2}$, in the 0.08 – 2.9 keV band (Voges et al. 1999), which provides evidence that the galaxy does not host a strong AGN. However, the host galaxy is detected in the Very Large Array Faint Images of the Radio Sky at Twenty-cm survey (FIRST; Becker, White & Helfand 1995), with 1.4 GHz flux density of 2.96 ± 0.15 mJy, corresponding to a luminosity of $L_{1.4GHz} \sim 2.6 \times 10^{21}$ W Hz $^{-1}$. If this radio emission were caused by star formation, the far-IR-radio correlation would imply a FIR luminosity of $L_{FIR} \sim 3 \times 10^9 L_\odot$ (Yun, Reddy & Condon 2001). However, detections of the host in archival Wide-field Infrared Survey Explorer (WISE; Wright et al. 2010) data gives a *W3*-band magnitude of $m_{W3} = 12.367 \pm 0.439$, corresponding to a luminosity of $L_{W3} \sim 2 \times 10^7 L_\odot$. This implies that the FIR luminosity would need to be roughly two orders of magnitude greater than the mid-IR (MIR) luminosity in order to reach the expected value if the radio emission was caused by star

formation. In addition, if the galaxy exhibited the strong star formation implied by this radio emission, we would expect to see additional signs of star formation, such as strong [O II] 3727Å emission, which we do not see in the host spectrum (see Figure 3). Thus, the radio emission from the host is likely not related to star formation, but may instead be an indicator of nuclear activity. However, the galaxy has a mid-IR (MIR) color of $(W1 - W2) \simeq 0.01 \pm 0.04$ in the WISE data, which, along with the non-detection in the X-ray data, provides evidence that any AGN activity is not strong (e.g., Assef et al. 2013).

Using the code for Fitting and Assessment of Synthetic Templates (FAST v1.0; Kriek et al. 2009), we fit stellar population synthesis (SPS) models to the 5'' SDSS *ugriz* and 2MASS *JHK_s* magnitudes of the host galaxy. The fit was made assuming a Cardelli, Clayton & Mathis (1988) extinction law with $R_V = 3.1$ and Galactic extinction of $A_V = 0.07$ mag based on Schlafly & Finkbeiner (2011), an exponentially declining star-formation history, a Salpeter IMF, and the Bruzual & Charlot (2003) models. We obtained a good SPS fit (reduced $\chi^2_\nu = 0.6$), with the following parameters: $M_* = (2.8^{+0.1}_{-0.1}) \times 10^9 M_\odot$, age = $1.3^{+0.2}_{-0.3}$ Gyr, and a 1σ upper limit on the star formation rate of $\text{SFR} \leq 0.9 \times 10^{-2} M_\odot \text{ yr}^{-1}$. In order to estimate the mass of the SMBH in PGC 043234, we use a bulge mass of $M_B \sim 10^{9.3} M_\odot$ based on the total mass from the FAST fit and Mendel et al. (2014) and the $M_B - M_{BH}$ relation from McConnell & Ma (2013), giving $M_{BH} \sim 10^{6.7} M_\odot$, a value very similar to that estimated for the host of ASASSN-14ae (Holoien et al. 2014a). We find no evidence for any significant additional extinction in fits to the transient spectral energy distribution (SED) despite the fact that the *Swift* UV data, particularly the *UVM2* band which lies on top of the 2200 Å extinction curve feature, is a powerful probe for additional dust. In the analyses event's SED which follow, we only correct for Galactic extinction.

We also retrieved an archival spectrum of PGC 043234 from SDSS DR9. The archival spectrum shows both [O III] 5007Å and [N II] 6584Å emission with luminosities of $L[\text{O III}] \sim 4.4 \times 10^5 L_\odot$ and $L[\text{N II}] \sim 3.6 \times 10^5 L_\odot$, respectively. As with the radio emission, this emission is likely not related to star formation, as the host shows no H α or [O II] in emission. Rather, this is again an indication that the host galaxy may host a low-luminosity AGN. However, the lack of X-ray emission and the MIR colors of the host from WISE imply that this nuclear activity is weak, as previously discussed.

The archival spectrum also shows H δ absorption with a large equivalent width, indicating a change in the galaxy's star formation history within the last ~ 1 Gyr (e.g. Goto et al. 2003). The strong H δ absorption indicates that the SED of the host is dominated by A stars, which implies that PGC 043234 may be a post-starburst galaxy (Goto et al. 2003). While some TDE hosts, such as NGC 5905, have shown evidence of nuclear star formation (Komossa & Greiner 1999), recent results from Arcavi et al. (2014) suggested that TDE candidates prefer post-starburst hosts, and PGC 043234 may follow this pattern. The relation between starbursts and TDEs will be further explored in a future paper on TDE hosts (Dong et al, *in prep.*).

2.2 New Photometric Observations

Following the discovery of the transient, we requested and were granted a series of 53 *Swift* XRT and UVOT target-of-opportunity (ToO) observations between 2014 November 30 and 2015 May 14. The UVOT observations were obtained in 6 filters: *V* (5468 Å), *B* (4392 Å), *U* (3465 Å), *UVM1* (2600 Å), *UVM2* (2246 Å), and *UW2* (1928 Å) (Poole et al. 2008). We extracted source counts from a 5'' radius region and sky counts from a $\sim 40''$ radius region using the UVOT software task UVOTSOURCE. We then used the most recent UVOT calibrations (Poole et al. 2008; Breeveld et al. 2010) to convert these count rates into magnitudes and fluxes.

The XRT operated in Photon Counting mode (Hill et al. 2004) during our observations. The data from all epochs were reduced with the software tasks XRTPIPELINE and XRTSELECT. We extracted X-ray source counts and background counts using a region with a radius of 20 pixels (47''.1) centered on the source position and a source-free region with a radius of 100 pixels (235''.7), respectively. In all epochs of observation, we detect X-ray emission consistent with the position of the transient. To convert the detected counts to fluxes, we assume a power law spectrum with $\Gamma = 2$ and Galactic H I column density (Kalberla et al. 2005).

The XRT data have an average detected count rate of 0.3 counts s^{-1} in the 0.3–10 keV range, corresponding to a flux of 3.0×10^{-11} ergs $\text{s}^{-1} \text{ cm}^{-2}$. This is roughly equivalent to a count rate of 1.2 counts s^{-1} in the ROSAT PSPC, indicating an increase by a factor of ~ 60 over the ROSAT limits.

In addition to the *Swift* XRT and UVOT observations, we also obtained *ugriz* images with the LT 2-m telescope and the LCOGT 1-m telescopes at Siding Spring Observatory, McDonald Observatory, Sutherland, and Cerro Tololo. We measured aperture photometry using a 5'' aperture radius in order to match the host galaxy and *Swift* measurements². We determined photometric zero-points using several SDSS stars in the field.

Figure 2 shows the X-ray, UV, and optical light curves of ASASSN-14li. The XRT flux measurements and UVOT/*ugriz* magnitudes are presented in Table A2 and Table A1, respectively. The observations cover the period from MJD 56983.6 (the epoch of discovery) through our latest epoch of observations on MJD 57161.9, spanning 178.3 days. The data are shown without extinction correction or host flux subtraction. Also shown in Figure 2 are the host magnitudes measured from SDSS images for *ugriz* and extrapolated from the host SED fit for *Swift* UVOT filters. Although our observations likely missed the peak of the transient's light curve, they still show that ASASSN-14li brightened considerably with respect to the host galaxy in the UV and blue filters, with the largest increase being in the *Swift* *UVM2* band, where it brightened by $\Delta m_{UVM2} \sim -4.1$. The *g*-band increase was significantly weaker, with $\Delta m_g \sim -0.4$.

² We attempted to do image subtraction of the follow-up *ugriz* data with the SDSS archival images as templates. However, due to the lack of stars in the field-of-view close to ASASSN-14li, the quality of the subtractions was sub-optimal and accurate measurements were not possible.

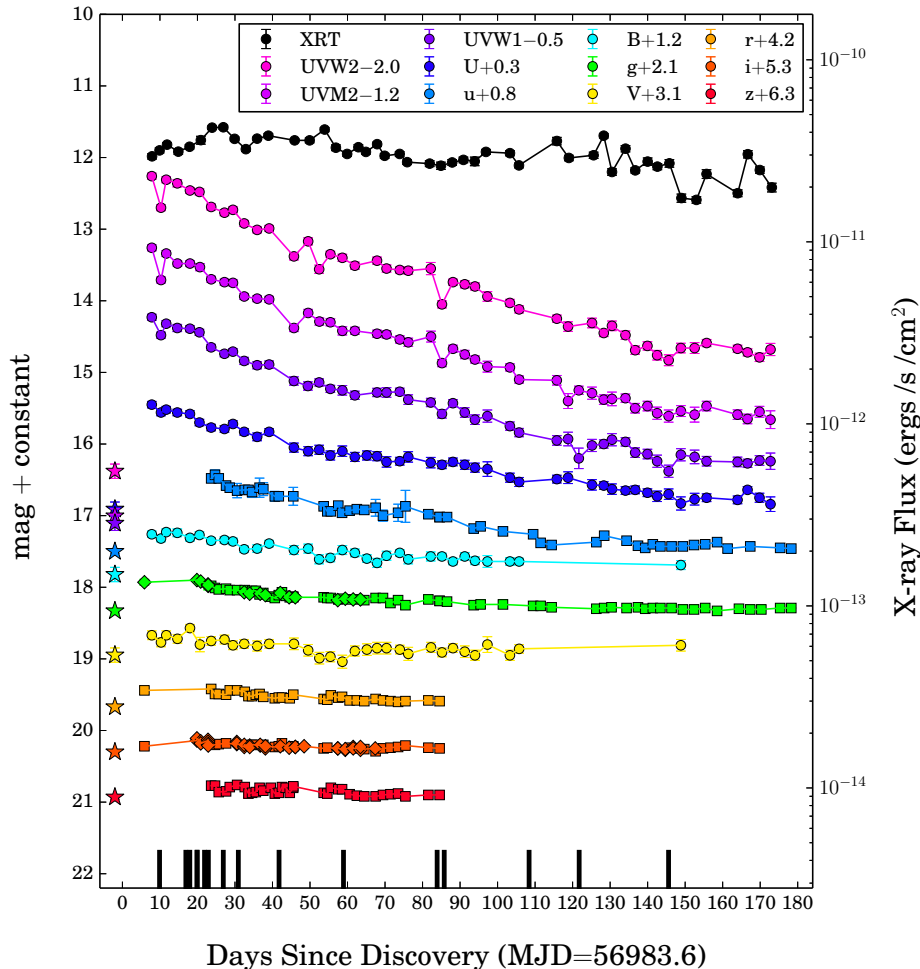


Figure 2. Light curves of ASASSN-14li beginning on the epoch of discovery (MJD= 56983.6) and spanning 178 days. Follow-up data obtained from *Swift* (X-ray, UV, and optical; circles), the LT 2-m (optical; squares), and the LCOGT 1-m telescopes (optical; diamonds) are shown as circles. All UV and optical magnitudes are shown in the Vega system (left scale), and X-ray fluxes are shown in ergs/s/cm^2 (right scale). The scales are chosen so that time variability has the same meaning for both the X-ray and optical/UV data. The data are not corrected for extinction and error bars are shown for all points, but in some cases they are smaller than the data points. Observations in the *riz* and *Swift BV* filters were terminated earlier than those in other bands, as the source had faded to be fainter than the host. $5''$ aperture magnitudes measured from archival SDSS images for *ugriz* and synthesized from our host SED model for the *Swift* UVOT filters are shown as stars at -5 days. Vertical bars at the bottom of the figure indicate dates of spectroscopic follow-up. Although the peak of the light curve was likely missed due to the source being in an unobservable position behind the Sun, the data still show that ASASSN-14li brightened considerably in the UV and in the bluer optical filters, with the largest increase being slightly more than 4 magnitudes in the *Swift* UVM2 band. Table A1 contains all the follow-up photometric data.

2.3 New Spectroscopic Observations

We obtained spectra of ASASSN-14li spanning 145 days between UT 2014 December 02 and UT 2015 April 14. The spectrographs used for these observations, along with wavelength range and resolution in angstroms, were: SNIFS mounted on the 2.2-m University of Hawaii telescope (3200–10000 Å, $R \sim 3$ Å), the Dual Imaging Spectrograph (DIS) mounted on the Apache Point Observatory 3.5-m telescope (range 3500–9800 Å, $R \sim 7$ Å), the Multi-Object Double Spectrographs (MODS; Pogge et al. 2010) mounted on the dual 8.4-m Large Binocular Telescope (LBT) on Mount Graham (3200–10000 Å, $R \sim 3$ Å), the Modular Spectrograph (Modspec) mounted on the MDM Observatory Hiltner 2.4-m telescope (4660–6730 Å, $R \sim 4$ Å), the Ohio State Multi-Object Spectrograph (OSMOS; Martini et al.

2011) mounted on the MDM Observatory Hiltner 2.4-m telescope (4200–6800 Å, $R \sim 4$ Å), the Fast Spectrograph (FAST; Fabricant et al. 1998) mounted on the Fred L. Whipple Observatory Tillinghast 1.5-m telescope (3700–9000 Å, $R \sim 3$ Å), and the Inamori Magellan Areal Camera and Spectrograph (IMACS; Dressler et al. 2011) mounted on the Las Campanas Observatory Magellan-Baade 6.5-m telescope (3650–9740 Å, $R \sim 8$ Å). The spectra from MODS were reduced using a custom pipeline written in IDL³ while all other spectra were reduced using standard techniques in IRAF. Telluric corrections were applied to the spectra using the spectra of spectrophotometric standard stars observed on

³ <http://www.astronomy.ohio-state.edu/MODS/Software/modsIDL/>

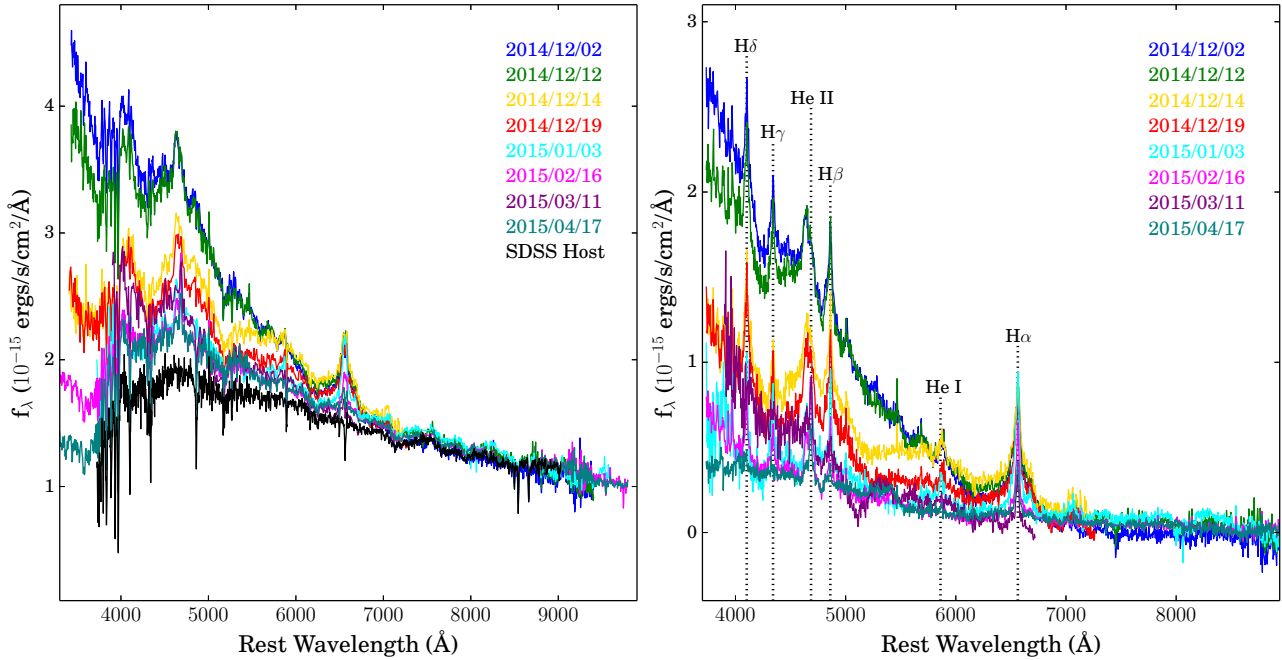


Figure 3. *Left Panel:* Spectral time-sequence for ASASSN-14li. Colors indicate the dates of observation. The archival SDSS spectrum of PGC 043234 is plotted in black. *Right Panel:* Host-galaxy-subtracted spectral time-sequence of ASASSN-14li, showing the same spectra used in the left panel with the host galaxy spectrum subtracted. Prominent emission lines in the transient spectrum, including Balmer lines, He I 5725Å, and He II 4686Å, are indicated by vertical dotted lines. The transient spectra show many broad emission features and blue continuum emission above that of the host at wavelengths shorter than ~ 4000 Å in all epochs.

the same nights. We calculated synthetic r -band magnitudes and scaled each spectrum to match the r -band photometry. Figure 3 shows a time-sequence of selected flux-calibrated follow-up spectra along with the archival SDSS spectrum of the host as well as a time-sequence of the same spectra with the host galaxy spectrum subtracted. Summary information, including dates, instruments used, and exposure times for all follow-up spectra, are listed in Table A3.

The key characteristics of the spectra of ASASSN-14li are a strong blue continuum, consistent with the photometric measurements, and the presence of broad Balmer and helium lines in emission, which are either absent or seen as absorption features in the host spectrum. The emission features are highly asymmetric and have widths of $\sim 10,000 - 20,000$ km s $^{-1}$ in all epochs, though they appear to grow narrower over time. The blue continuum becomes progressively weaker over time, though it still shows emission in excess of the host at wavelengths shorter than ~ 6000 Å in the latest epoch, which is in agreement with the UV and optical photometry. We further analyze the features of these spectra and compare to ASASSN-14ae and other TDE candidates in §3.2.

3 ANALYSIS

3.1 SED Analysis

Using the $5''0$ aperture magnitudes measured from the archival SDSS data and synthesized from the FAST SED fit for *Swift* UVOT filters we performed host flux subtraction

on the extinction-corrected photometric follow-up data. We then used these host-subtracted fluxes to fit the SED of ASASSN-14li with blackbody curves using Markov Chain Monte Carlo (MCMC) methods, as was done for ASASSN-14ae in Holoien et al. (2014a). As flux in redder filters was clearly dominated by host flux even in early epochs, we only use filters with effective wavelength less than 4000 Å (*Swift* U , $UVW1$, $UVM2$, and $UVW2$ and SDSS u) when fitting the SED. Unlike ASASSN-14ae, the UV data for ASASSN-14li do not appear to span the peak of the SED, resulting in a broad range of possible blackbody temperatures. If we use a very weak temperature prior (± 1 dex), the median epoch with measurements at four or more wavelengths has a formal temperature uncertainty of ± 0.2 dex. However, without a clear detection of the spectral peak, temperature uncertainties are likely dominated by systematic errors (e.g. host flux or deviations of the true spectral shape from a black body) rather than this estimate of the statistical errors. We therefore adopted a temperature typical of these weakly constrained fits and a strong prior of $\log T/K = 4.55 \pm 0.05$ for our standard fits. The evolution of the source's SED along with the best-fit blackbody curves are shown in Figure 4.

With the temperature constrained by our prior to remain roughly constant, the optical/UV luminosity of the source fades steadily over the ~ 178 days after initial discovery. The luminosity evolution is well fit by an exponential curve $L \propto e^{-t/t_0}$ with $t_0 \simeq 60$ days, as shown in Figure 5. This differs from common TDE models, where the luminosity evolution is expected to follow a power law t^{-x} with $x \simeq 5/12 - 5/3$ (e.g., Strubbe & Quataert 2009; Lodato & Rossi 2011). However, the exponential luminosity evolution

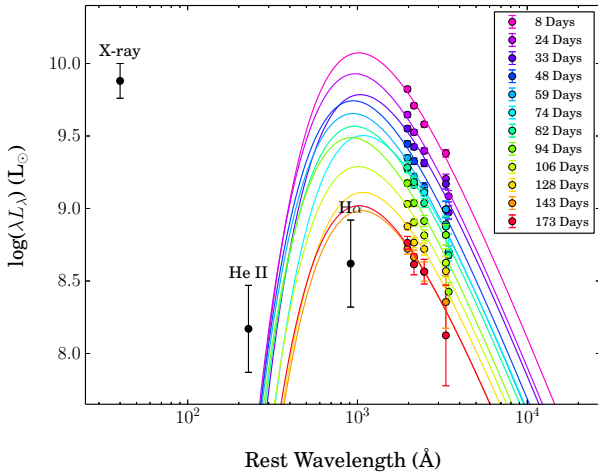


Figure 4. Evolution of the SED of ASASSN-14li shown in different colors (points) and the corresponding best-fitting blackbody models for each epoch (lines). Only data points with subtracted flux greater than 0.3 times the host flux are shown, as data points with a smaller fractional flux were highly uncertain and contributed little to the fit. All data points have been corrected for Galactic extinction and include error bars, though in some cases the error bars can be smaller than the data points. All fits were made assuming a temperature prior of $\log T/K = 4.55 \pm 0.05$. Also shown are the early-epoch X-ray luminosity and ionizing luminosities implied by the H α and He II 4868Å lines (see § 3.2.) No additional UV emission is required to produce the line emission, but the X-ray emission is likely non-thermal or produced in a separate, hotter region.

matches that of ASASSN-14ae, the other ASAS-SN TDE (Holoien et al. 2014a), meaning that this behavior is consistent with previously discovered TDE candidates. This temperature and luminosity behavior is inconsistent with what would be expected if ASASSN-14li were a supernova (which typically show rapidly declining temperatures along with constant or declining luminosity (e.g., Miller et al. 2009; Botticella et al. 2010; Inserra et al. 2013; Graham et al. 2014), providing evidence that ASASSN-14li is a better match to a TDE than a supernova.

The X-ray luminosity, by contrast, declines at a much slower rate than the optical/UV luminosity, and roughly 40 days after discovery the X-ray luminosity becomes the dominant source of emission. As shown in Figure 4, the X-ray luminosity requires a significantly higher blackbody temperature (roughly $T \sim 10^5$ K) than the $T \sim 35,000$ K temperature that best-fits the optical/UV data. While we cannot rule out a single blackbody component with much higher temperature generating both the optical/UV and the X-ray emission, we believe it is more likely that the X-ray emission arises from a different, hotter region of the source seen through a region of lower-than-average density, as described in Metzger & Stone (2015), or that it is non-thermal.

Integrating over the X-ray and optical/UV luminosity curves using only epochs with *Swift* UV data implies that ASASSN-14li radiated a total energy of $E \simeq 7 \times 10^{50}$ ergs over the time period covered by our follow-up data. This requires accretion of only $\Delta M \sim 4.0 \times 10^{-3} \eta_{0.1}^{-1} M_{\odot}$ of mass, where $\eta_{0.1} = 0.1\eta$ is the radiative efficiency, to power the event.

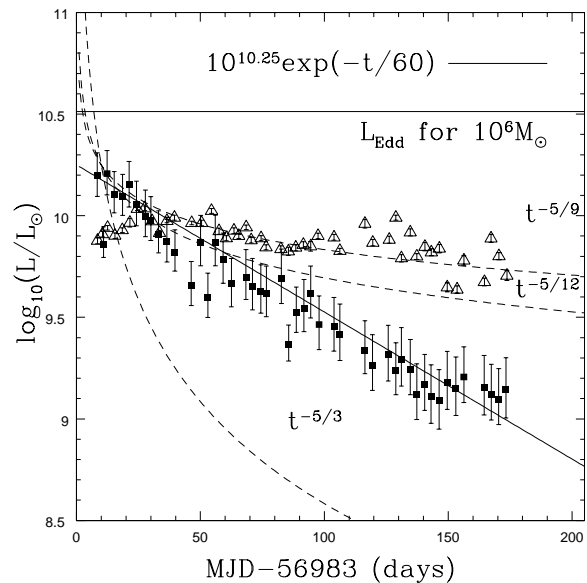


Figure 5. Evolution of ASASSN-14li’s luminosity over time. Open triangles indicate the X-ray luminosity measurements. Dashed lines show popular power law fits for TDE luminosity curves $L \propto t^{-x}$ (e.g., Strubbe & Quataert 2009; Lodato & Rossi 2011) while the diagonal solid line shows an exponential fit. The Eddington luminosity for a $M = 10^6 M_{\odot}$ black hole is shown as a solid horizontal line. The luminosity evolution appears to be best-fit by the exponential model, similar to the previous ASASSN TDE candidate, ASASSN-14ae (Holoien et al. 2014a).

3.2 Spectroscopic Analysis

In their analysis of TDE candidates discovered by the Palomar Transient Factory, Arcavi et al. (2014) found that all their candidates showed similar spectroscopic characteristics, including a strong blue continuum, and that their candidates spanned a continuum from H-rich to He-rich spectroscopic features. The follow-up spectra of ASASSN-14li show many of the same characteristics as the TDEs that Arcavi et al. (2014) refer to as “intermediate H+He events,” because its spectra have strong He and H emission features in all epochs. In Figure 6 we compare the spectra of ASASSN-14li to ASASSN-14ae from Holoien et al. (2014a) at similar epochs after discovery. The spectra are broadly similar, as expected, with both showing strong emission at bluer wavelengths and broad H α emission features, but there are some notable differences. The blue continuum seems to fade somewhat more slowly in ASASSN-14li than in ASASSN-14ae, and ASASSN-14li shows a broad He II 4686 Å emission feature even in early epochs (a few days after discovery), whereas ASASSN-14ae only began to show this feature a few months after discovery. We note that some of these differences could stem from the fact that ASASSN-14li was further past its peak luminosity when discovered than ASASSN-14ae was (the previous non-detection of ASASSN-14ae was roughly 3 weeks prior to discovery, whereas ASASSN-14li was not observed for nearly 3 months before being discovered). However, given the range of TDE candidate properties found by Arcavi et al. (2014), it is likely that some of the differences observed between these objects are unrelated to their age.

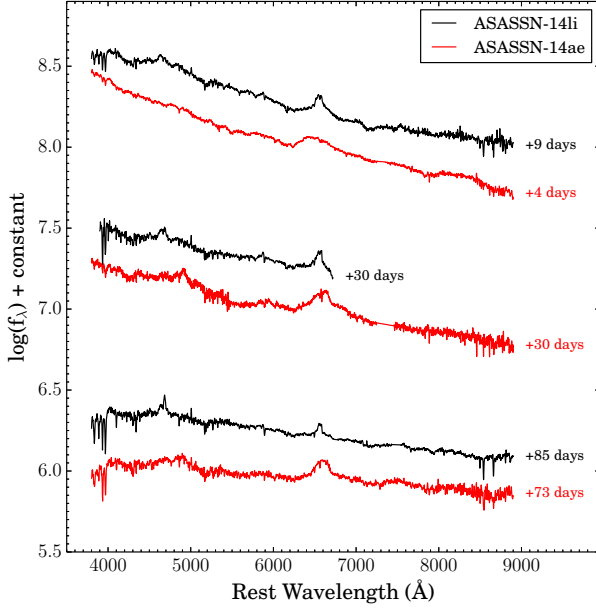


Figure 6. Comparison of the spectra of ASASSN-14li with those of ASASSN-14ae (Holoien et al. 2014a) at similar epochs after discovery. ASASSN-14li is shown in blue while ASASSN-14ae is shown in red, and epochs in days-after-discovery are shown to the right of each spectrum. The spectra look broadly similar, with both objects showing a strong blue continuum that declines over time and a broad H α emission feature in all epochs. However, the spectra of ASASSN-14li also show a strong He II 4686 Å emission feature in all epochs, whereas ASASSN-14ae only begins to show He II emission in later epochs.

In Figure 7 we show the luminosity evolution of three strong emission features (H α , H β , and He II 4686 Å) present in the spectra of ASASSN-14li. As estimating the true error on these fluxes is difficult given their complex shape, we assume 20% errors on the emission fluxes calculated in each epoch. The three lines span a wide range in luminosity in early spectra, with peak values of $L_{H\alpha} \sim 1.1 \times 10^{41}$ ergs s $^{-1}$, $L_{H\beta} \sim 4.0 \times 10^{40}$ ergs s $^{-1}$, and $L_{He II} \sim 8.5 \times 10^{40}$ ergs s $^{-1}$. However, the more luminous lines also appear to decline in luminosity more quickly, such that by the time of our most recent spectra, all three lines have luminosities in the range $L \sim (0.5 - 1.5) \times 10^{40}$ ergs s $^{-1}$. In Figure 7 we also show the H α emission expected given the measured H β emission assuming the emission is driven by case B recombination. Within noise, the H α /H β ratio seems to be largely consistent with recombination. The measured luminosities for all three lines are given in Table A4.

We also compare the evolution of the H α and He II 4686 Å line profiles of ASASSN-14li to those of ASASSN-14ae in Figure 8, spanning the period from 9 days after discovery to 145 days after discovery for ASASSN-14li and from 4 days after discovery to 132 days after discovery for ASASSN-14ae. While both objects show strong emission features, the evolution of these features shows a number of differences between the two objects. The H α profile is fairly asymmetric and narrows over time for both objects. However, ASASSN-14li shows a significantly narrower H α emission feature than ASASSN-14ae in all epochs. At 9 days, the ASASSN-14li H α feature shows a narrow peak and has

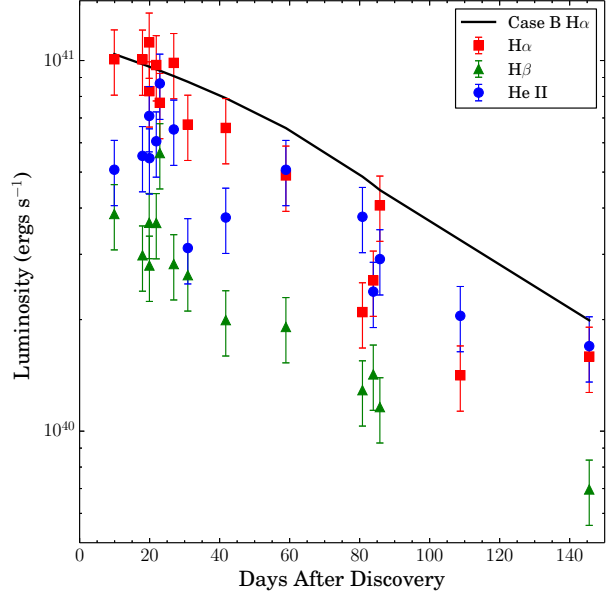


Figure 7. Evolution of the H α (red squares), H β (green triangles), and He II 4686 Å (blue circles) luminosities. Errorbars show 20% errors on the line fluxes. The black line shows the H α emission that would be expected from case B recombination, given the H β emission. The H α emission is generally consistent with recombination.

blue/red wings reaching $\sim -10,000/+10,000$ km s $^{-1}$ at the base of the line, while at 4 days the ASASSN-14ae H α feature shows a broad peak and has blue/red wings reaching $\sim -15,000/+10,000$ km s $^{-1}$. The H α feature becomes significantly narrower for both objects by the time of the latest spectroscopic epoch, with ASASSN-14li showing blue/red wings reaching $\sim -5,000/+5,000$ km s $^{-1}$ and ASASSN-14ae showing blue/red wings reaching $\sim -5,000/+10,000$ km s $^{-1}$. The FWHM of the two lines show a similar evolutionary trend, with the H α feature narrowing from FWHM $\simeq 3,000$ km s $^{-1}$ to FWHM $\simeq 1,500$ km s $^{-1}$ for ASASSN-14li and from FWHM $\simeq 17,000$ km s $^{-1}$ to FWHM $\simeq 8,000$ km s $^{-1}$ for ASASSN-14ae. Given the fact that “later” epochs of ASASSN-14ae seem to resemble “earlier” epochs of ASASSN-14li, the H α evolution suggests that ASASSN-14li may have been older than ASASSN-14ae at discovery. However, the uncertainty on the age of ASASSN-14li is not so great as to suggest that all these differences are strictly due to the age of the transient.

The two TDE candidates show more obvious differences in the evolution of their He II 4686 Å line profiles. As can be seen in Figure 8, ASASSN-14li displays a strong He II emission feature in all epochs, while ASASSN-14ae only begins to show a similar feature in later spectra. The He II feature shows similar evolution to the H α feature for ASASSN-14li, as it is fairly asymmetric in all epochs and narrows over time, with the 9-day spectrum showing blue/red wings reaching $\sim -10,000/+5,000$ km s $^{-1}$ and the 145-day spectrum showing blue/red wings reaching $\sim -5,000/+3,000$ km s $^{-1}$. ASASSN-14ae does not show a He II feature in the 4-day spectrum, but its latest spectrum taken at 132 days after discovery shows a feature that resembles that of ASASSN-14li, with blue/red wings reaching $\sim -5,000/+3,000$ km s $^{-1}$.

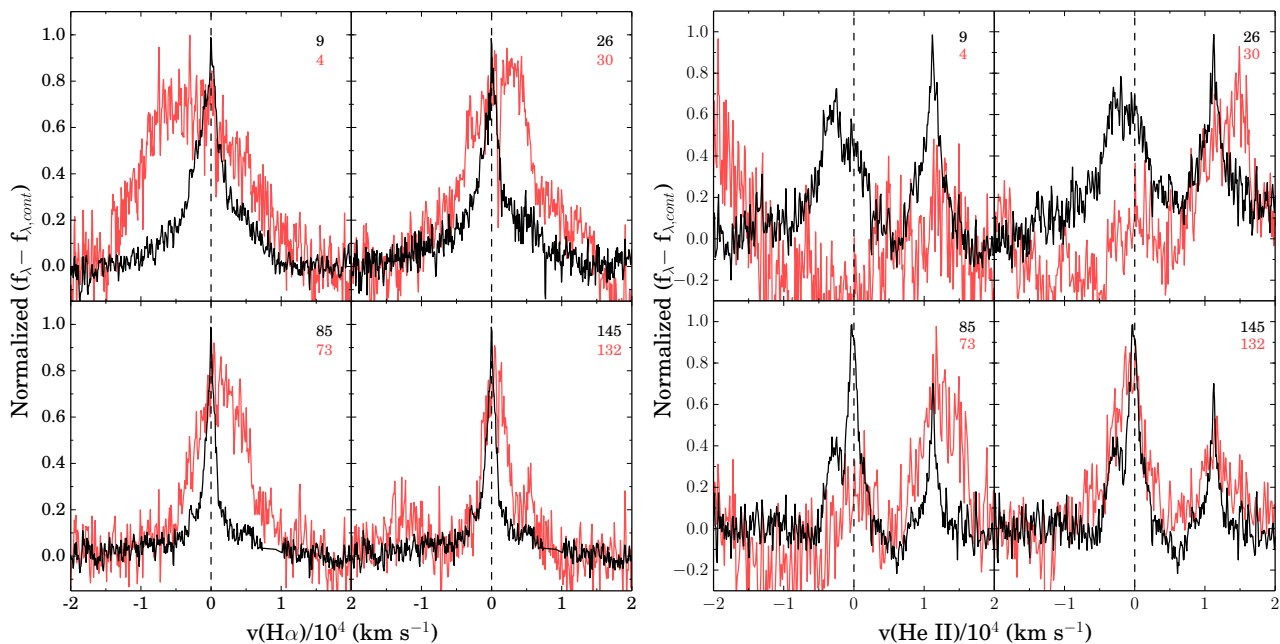


Figure 8. Evolution of the H α (left panel) and He II 4686 Å (right panel) line profiles of ASASSN-14li (black) and ASASSN-14ae (red; Holoien et al. 2014a). (The strong line to the right of the He II 4686 Å line in the right panel is H β .) The number of days since discovery for each spectrum is shown in the upper-right corner of each panel, with colors matching the colors of the spectra. We have subtracted the host galaxy spectra and a locally defined low-order continuum around the lines from each spectrum. Both objects show an asymmetric H α profile that narrows over time, with ASASSN-14li showing a significantly narrower profile than ASASSN-14ae in all epochs. ASASSN-14li shows a similar He II profile that also narrows over time in all epochs, while ASASSN-14ae only shows significant He II emission at later epochs. The He II profile of ASASSN-14li shows two velocity peaks, one at 0 km s $^{-1}$ and one at ~ -2000 km s $^{-1}$, which evolve in their relative intensity over time.

Finally, we examine the evolution of the emission line widths, shown in Figure 9 for H α . As the luminosity of the transient is decreasing, so too is the line width. This is the opposite of what is seen in reverberation mapping studies of quasars, where estimates of the black hole mass $M_{BH} \propto \Delta v^2 L^{1/2}$ remain roughly constant because the luminosity decreases as the line width broadens (e.g., Peterson et al. 2004; Denney et al. 2009). Physically, this is believed to result from the fact that if the luminosity drops, gas at larger distances and lower average velocities recombines, leading to an increase in the line width.

Simple estimates based on the line luminosities and light travel times imply that the densities of the ionized regions of ASASSN-14li are also high enough to make the recombination times negligible. This means it is unlikely that the narrowing of the lines is due to a finely-tuned outward density gradient allowing the higher velocity material at smaller radii to recombine faster while also making the line width shrink with time. The fast recombination times also make it difficult to explain the decreasing line widths as simply being due to a continuing expansion of the Stromgren sphere even as the luminosity is decreasing.

No TDE has been caught early enough to make these measurements, but there should be temporal lags between the rise of the UV emission and the formation of the broad lines, as is seen in reverberation mapping of AGN (e.g., Peterson et al. 2004). At late times, these effects are still present, but seem an unlikely explanation for the observed

line width evolution, as the temporal smoothing of the changes becomes larger when the delays are long.

A final possibility is that the changes represent evolution in the density distribution of the ionized gas. While there is no reason to expect rapid, large scale gas redistributions in a normal AGN, such changes seem plausible during a TDE. This is presumably not a large scale redistribution, since the time scale for a significant change in radius is $t \sim 50 M_{BH7} v_3^{-3}$ years, where $M_{BH7} = (10^7 M_\odot) M_{BH}$ and $v_3 = (3,000 \text{ km s}^{-1}) v$. It would not be surprising, however, to have significant evolution in the mean density at a given radius given the nature of a TDE. For example, if the line emission is dominated by a dense gas phase, but the average density of this phase is decreasing, the total line emission diminishes in proportion to the density. Given the quality of the spectra of ASASSN-14li, we do not attempt any quantitative analysis, but these questions suggest a need for higher quality spectra in future studies of TDEs.

The spectra of ASASSN-14li seem to be consistent with both those of ASASSN-14ae and those of other TDE candidates in literature, showing strong emission at bluer wavelengths that fades steadily over time and strong Balmer and helium emission features in all epochs. These similarities, as well as the fact that these spectra do not seem to resemble those of type II supernovae or AGN, provide strong evidence for a TDE interpretation for ASASSN-14li.

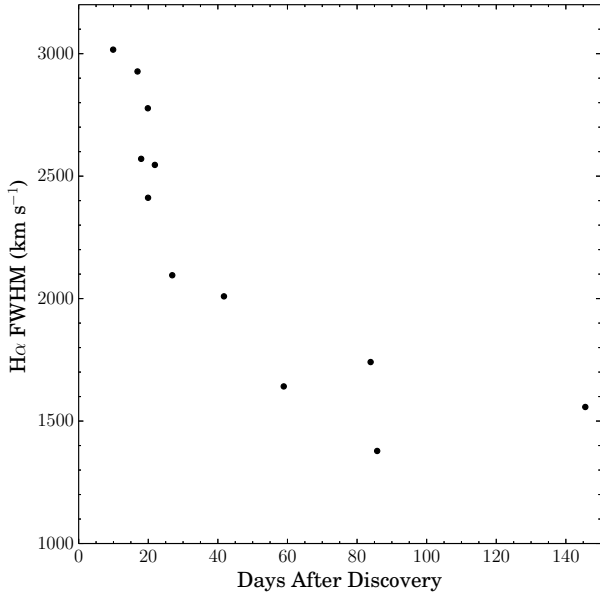


Figure 9. Evolution of the H α line width. As the luminosity of the line also decreases with time (see Figure 7), the line is becoming narrower as the luminosity decreases. This is the opposite of what is seen in reverberation mapping studies of quasars.

4 TDE RATES

Due to the small number of candidate TDEs, the rate of stellar tidal disruptions by SMBHs is not particularly well-understood. This rate may be important, however, as it can be used to study the orbits of stars around SMBHs and the origin of relativistic TDEs that have been observed with *Swift* (van Velzen & Farrar 2014). Furthermore, if the rate is high enough, it may even play an important role in the growth of SMBHs (e.g., Magorrian & Tremaine 1999). Van Velzen & Farrar (2014) used four TDE detections (two from SDSS and two from Pan-STARRS) and a search of SDSS Stripe 82 galaxies to estimate a TDE rate of $(1.5-2.0)_{-1.3}^{+2.7} \times 10^{-5} \text{ yr}^{-1}$ per galaxy. In Holoien et al. (2014a) we used estimates for the local density of black holes from Shankar (2013) and an observable volume of $3 \times 10^7 \text{ Mpc}^3$ for ASAS-SN to estimate that ASAS-SN would discover 0.3 – 3 TDEs per year, assuming a 50% detection efficiency. If we take our estimate of 50% detection efficiency to be true, the fact that ASAS-SN discovered 2 TDE candidates in 2014 would imply that the actual rate of tidal disruptions is actually much higher than the estimate from van Velzen & Farrar (2014), possibly as high as $\sim 10^{-4} \text{ yr}^{-1}$ per galaxy. However, the assumption of a 50% detection efficiency is arbitrary, and as the rate estimate depends strongly on this quantity, a more realistic simulation of the ASAS-SN detection efficiency is needed.

To make a more quantitative estimate of the TDE rate, we used SDSS galaxies, which includes the hosts of both of our TDE candidates. We selected all galaxies from SDSS DR9 with $0.01 < z < 0.10$, no duplicate spectra, and with photometric data. We randomly assigned all $N_g = 348853$ galaxies an integer code from 1 to 100 and extracted aperture light curves for the centers of a randomly selected 4% of these galaxies. We analyzed all light curves from 2014 January 1 to 2015 May 1.

We modeled the peak of the light curve, which will dominate any magnitude limited detections, as $M_V = V_{peak} + (t - t_0)^2/t_1^2$ where V_{peak} is the peak absolute magnitude, t_0 is the time of peak, and t_1 is the time to decay by one magnitude from the peak. For each galaxy, these were converted to apparent magnitudes using a quadratic fit to the luminosity distance for an $H_0 = 70 \text{ km s}^{-1} \text{ Mpc}^{-1}$, $\Omega_0 = 0.3$, $\Omega_\Lambda = 0.7$ flat cosmological model combined with the Galactic extinction in each sightline. For each galaxy, $N_t = 1000$ trial values of t_0 were drawn from one month before the start of the light curve to one month afterward for a total time span of Δt_m , and the trial source was viewed as detected if there would be two signal-to-noise ratio $S/N > 7.5$ detections within one week given the model and the estimated noise in the actual light curve for the center of the galaxy. This criterion detects both of our observed candidates. With these definitions, the survey time over which we would detect a TDE in any single galaxy is $\Delta t = \Delta t_m N_d / N_t$, where N_d is the number of trial detections. Averaging this over all the trial galaxies gives us a mean survey time per galaxy $\langle \Delta t \rangle$, leading to a rate estimate of

$$r = \frac{N_{TDE}}{N_g \langle \Delta t \rangle}. \quad (1)$$

The results as a function of V_{peak} and t_1 are presented in Table 2. We have not included results for transients fainter than $V_{peak} = -18$ mag because they begin to be significantly affected by the $z > 0.01$ redshift cutoff.

Using ASASSN-14ae (Holoien et al. 2014a) and PS1-10jh (Gezari et al. 2012) as examples of “typical” TDEs, we assume that typical TDEs have $V_{peak} \simeq -19$ to -20 and decay by one magnitude in 25 to 40 days. In Table 2, we see that the time scale t_1 has only a modest affect on the effective survey time once $t_1 > 10$ days, while the peak magnitude has an enormous effect because it controls the effective survey volume. If we assume that TDEs are uniformly distributed over the $V_{peak} = -19$ and -20 mag bins for $t_1 = 20, 30$ and 40 days, we find that $N_g \langle \Delta t \rangle \simeq 49,000$ years implying an average TDE rate of $r \simeq 4.1 \times 10^{-5} \text{ yr}^{-1}$ per galaxy given $N_{TDE} = 2$. The Poisson uncertainties correspond to a 90% confidence range of $(2.2 - 17.0) \times 10^{-5} \text{ yr}^{-1}$ per galaxy, and these probably dominate over the systematic uncertainties. For example, the fractional shifts from taking any of the cases averaged over to yield the estimate of $N_g \langle \Delta t \rangle$ are significantly smaller than the Poisson uncertainties. This rate estimate is higher than the rate of $(1.5 - 2.0)_{-1.3}^{+2.7} \times 10^{-5} \text{ yr}^{-1}$ per galaxy found by van Velzen & Farrar (2014), though the two estimates are consistent given the uncertainties. If we lower the threshold to two observations with $S/N > 5$, the rate estimate drops by a factor of 1.5 and is closer to the estimate of van Velzen & Farrar (2014), but the predicted magnitude distribution of Type Ia SN for this threshold is somewhat fainter than is observed. If we raise the threshold to $S/N > 10$, the rate estimate rises by a factor of 1.4 and is closer to theoretical predictions (e.g., Stone & Metzger 2014; Metzger & Stone 2015), but the predicted magnitude distribution of Type Ia SN is somewhat brighter than is observed and the two TDEs no longer satisfy the detection criterion.

5 DISCUSSION

ASASSN-14li, discovered by ASAS-SN on 2014 November

Table 2. Detection Statistics

V_{peak}	t_1 (days)	$\langle\Delta t\rangle$ (days)	$N_g\Delta t$ (years)
-18	10	4.88	4661
	20	6.31	6028
	30	7.11	6793
	40	7.70	7351
-19	10	20.51	19588
	20	25.48	24331
	30	28.53	27251
	40	30.68	29307
-20	10	55.78	53280
	20	67.77	64730
	30	75.13	71753
	40	80.60	76980
-21	10	131.82	125903
	20	159.56	152400
	30	176.58	168655
	40	189.30	180803

For a given transient peak V_{peak} and time to decay one magnitude t_1 , Δt is the average number of days per galaxy in which the transient would be detected, leading to a total survey time of $N_g\Delta t$ where $N_g = 348853$ is the total number of $0.01 < z < 0.1$ SDSS galaxies we considered.

11, had a position consistent to within 0.17 ± 0.21 arcseconds of the center of PGC 043234 and a peak absolute V -band magnitude of $M_V \sim -19$. Follow-up observations indicate that it is not consistent with either a supernova or a normal AGN outburst. Conversely, it shows many similarities with other TDE candidates discovered by optical surveys. ASASSN-14li has remained bright in the UV and blue optical filters even six months after detection, and the best-fit blackbody temperature has remained roughly constant at $T \sim 35,000$ K for the duration of the outburst while the luminosity has declined at a steady rate best fit by an exponential decay curve. Spectra of ASASSN-14li show a strong blue continuum and broad Balmer and helium emission features in all epochs, and do not show the spectral evolution expected of supernovae or AGN. Such features are characteristic of TDE candidates such as those discovered by ASAS-SN (ASASSN-14ae, Holoien et al. 2014a) and iPTF (Arcavi et al. 2014), which leads us to the conclusion that ASASSN-14li was likely a TDE as well. Its proximity ($z = 0.0206$) makes it the closest TDE candidate discovered at optical wavelengths to date, and it is also the first TDE candidate discovered at optical wavelengths to exhibit both UV/optical emission as well as associated X-ray emission.

Archival spectroscopy and photometry, as well as SED fitting, indicate that the transient host galaxy PGC 043234 has undergone a change in its star formation history within the last ~ 1 Gyr and has a stellar population dominated by A stars, implying that it is a post-starburst galaxy. Previous work by Arcavi et al. (2014) indicated that TDE candidates may prefer such hosts, and this possibility will be further explored in future work on ASAS-SN TDE host galaxies (Dong et al., *in prep.*). The host does not show signs of recent star formation, and while the detection of [O III] emission and radio emission may imply that it hosts a weak AGN, its

mid-IR colors from WISE are inconsistent with significant AGN activity.

ASASSN-14li has significantly more HeII emission than ASASSN-14ae, so much so that the HeII Stromgren sphere is likely of comparable size to the H Stromgren sphere. This is consistent with the diversity of He and H line strengths noted by Arcavi et al. (2014). The observed soft UV SEDs, line luminosities, and X-ray properties of the two ASASSN TDE candidates also provide a natural explanation of the diversity. ASASSN-14li has both a harder soft UV continuum and significant X-ray flux, which implies a stronger hard/ionizing UV continuum. This is then observed indirectly through the greater ratio of He to H emission in the spectra. While the unknown covering fractions mean that the observed line luminosities only set lower bounds on the hard UV continuum, their ratios likely provide reasonable estimates of the spectral slopes because it is difficult to make the H and He line emission regions enormously different.

The evolution of the line widths is also interesting, as discussed in more detail in § 3.2. For the “quiescent” environments of reverberation mapped AGN, decreases in luminosity are accompanied by increases in line widths (e.g. Peterson et al. 2004; Denney et al. 2009). For ASASSN-14li we see the opposite: as the transient fades, the line widths become narrower. One likely explanation for this behavior is that the line width evolution is due to more rapid evolution of the density distribution closer to the black hole. We do not mean in the sense of large scale changes in the amount of mass at a given radius – for the typical velocities of the lines ($1,000\text{--}3,000$ km s $^{-1}$), this occurs relatively slowly (years to decades) if the velocities are virialized. However, rearrangements of the gas that change the mean emission measure can occur much more rapidly, so the line evolution may provide a probe of the evolution of the “clumpiness” of the material on these velocity scales.

Both of these issues are worth exploring in more detail, but they also need higher quality spectra than we have available for ASASSN-14li. Spectra with significantly higher signal-to-noise ratios obtained at a higher cadence are needed to closely track the evolution of the structure of the emission lines. In such a close study it will be important to bear in mind the effects of light travel times (days to months), potentially with the possibility of essentially carrying out a reverberation mapping study of a TDE. This would also require a high cadence continuum light curve including the onset of the transient.

We used SDSS galaxies including the hosts of the two TDE candidates discovered by ASAS-SN to estimate the rate of tidal disruptions in galaxies with redshift $0.01 < z < 0.10$. We extracted aperture light curves from the centers of randomly selected galaxies to model the completeness. Assuming that TDEs are uniformly distributed between $V_{peak} = -19$ and $V_{peak} = -20$ and have a characteristic decay time between 20, 30 and 40 days (roughly consistent with most TDE candidates in literature), we find a 90% confidence range of $r = (2.2 - 17.0) \times 10^{-5}$ yr $^{-1}$ per galaxy given the two ASAS-SN TDE candidates discovered between 2014 January 1 and 2015 May 1. This rate is in agreement with the rate found by van Velzen & Farrar (2014) in their analysis of SDSS TDE candidates, though our average rate estimate is higher, and will be further refined in future work by Dong et al. (*in prep.*).

We also note that if we carry out a similar rate analysis for Type Ia SNe in ASAS-SN, we find a rate consistent with that found by the LOSS survey (Li et al. 2011), suggesting that the overall analysis is reasonably robust. A detailed analysis of Type Ia rates in ASAS-SN will be carried out in a future publication by Holoien et al. (*in prep.*).

TDEs and Type Ia SNe have broadly similar peak magnitudes and time scales at peak, so we would naively expect the two source types to have similar selection effects and hence ratios of event numbers between surveys. For ASAS-SN, this ratio is approximately 1 TDE for every 70 Type Ia SNe (2 and 135, respectively). The ratios for PTF (Arcavi et al. 2014; Rau et al. 2009), Pan-STARRS and SDSS (Gezari et al. 2012; Chornock et al. 2014; van Velzen & Farrar 2014) are 1 TDE for every 550, 1000, and 1050 SNe Ia, respectively.⁴ Unless we have been unusually lucky (for the PTF/Pan-STARRS/SDSS ratios, we would have a 1-2% probability of finding two TDEs), this comparison suggests the (testable) possibility that the completeness of TDE searches in ASAS-SN is markedly higher than in prior surveys. This offers the exciting possibility that a much larger population of TDEs can be identified in existing surveys, although the sample found by ASAS-SN will remain the most useful for detailed study due to their intrinsic brightness. It remains to be seen, however, if this will help explain the gap between observed and theoretical TDE rate estimates (see Metzger & Stone 2015).

ASASSN-14li is the closest TDE candidate ever discovered at optical wavelengths, and it has been extensively observed for over 6 months since discovery, resulting in an unprecedented data set spanning optical to X-ray wavelengths. Given the design of the ASAS-SN survey, future TDE candidates that we discover will be similarly easy to observe with a variety of telescopes and instruments, allowing us to develop a catalog of well-studied TDE candidates that can be used for population studies and to study the early and late-time behaviors of these transients, which cannot be done with TDEs discovered at higher redshifts. With a planned expansion to 8 cameras in mid-2015, ASAS-SN will be an even more powerful tool for the discovery and study of TDEs and other bright transients in the future.

ACKNOWLEDGMENTS

The authors thank PI Neil Gehrels and the *Swift* ToO team for promptly approving and executing our observations. We thank D. Mudd for assistance with data analysis and R. Pogge for discussion. We thank LCOGT and its staff for their continued support of ASAS-SN.

Development of ASAS-SN has been supported by NSF grant AST-0908816 and the Center for Cosmology and AstroParticle Physics at the Ohio State University. ASAS-SN is supported in part by Mt. Cuba Astronomical Foundation.

TW-SH is supported by the DOE Computational Science Graduate Fellowship, grant number DE-FG02-97ER25308. Support for JLP is in part provided by FONDECYT through the grant 1151445 and by the Ministry of

Economy, Development, and Tourism’s Millennium Science Initiative through grant IC120009, awarded to The Millennium Institute of Astrophysics, MAS. SD is supported by the Strategic Priority Research Program-“The Emergence of Cosmological Structures of the Chinese Academy of Sciences (Grant No. XDB09000000)”. BJS is supported by NASA through Hubble Fellowship grant HST-HF-51348.001 awarded by the Space Telescope Science Institute, which is operated by the Association of Universities for Research in Astronomy, Inc., for NASA, under contract NAS 5-26555. JFB is supported by NSF grant PHY-1404311. PRW is supported by the Laboratory Directed Research and Development program at LANL.

This research has made use of the XRT Data Analysis Software (XRTDAS) developed under the responsibility of the ASI Science Data Center (ASDC), Italy. At Penn State the NASA *Swift* program is support through contract NAS5-00136.

This research uses data obtained through the Telescope Access Program(TAP), which has also been funded by the aforementioned Strategic Priority Research Program and the Special Fund for Astronomy from the Ministry of Finance.

Observations made with the NASA Galaxy Evolution Explorer (GALEX) were used in the analyses presented in this manuscript. Some of the data presented in this paper were obtained from the Mikulski Archive for Space Telescopes (MAST). STScI is operated by the Association of Universities for Research in Astronomy, Inc., under NASA contract NAS5-26555. Support for MAST for non-HST data is provided by the NASA Office of Space Science via grant NNX13AC07G and by other grants and contracts.

The Liverpool Telescope is operated on the island of La Palma by Liverpool John Moores University in the Spanish Observatorio del Roque de los Muchachos of the Instituto de Astrofísica de Canarias with financial support from the UK Science and Technology Facilities Council.

This research was made possible through the use of the AAVSO Photometric All-Sky Survey (APASS), funded by the Robert Martin Ayers Sciences Fund.

This research has made use of data provided by Astrometry.net (Barron et al. 2008).

Funding for SDSS-III has been provided by the Alfred P. Sloan Foundation, the Participating Institutions, the National Science Foundation, and the U.S. Department of Energy Office of Science. The SDSS-III web site is <http://www.sdss3.org/>.

SDSS-III is managed by the Astrophysical Research Consortium for the Participating Institutions of the SDSS-III Collaboration including the University of Arizona, the Brazilian Participation Group, Brookhaven National Laboratory, Carnegie Mellon University, University of Florida, the French Participation Group, the German Participation Group, Harvard University, the Instituto de Astrofísica de Canarias, the Michigan State/Notre Dame/JINA Participation Group, Johns Hopkins University, Lawrence Berkeley National Laboratory, Max Planck Institute for Astrophysics, Max Planck Institute for Extraterrestrial Physics, New Mexico State University, New York University, Ohio State University, Pennsylvania State University, University of Portsmouth, Princeton University, the Spanish Participation Group, University of Tokyo, University of Utah,

⁴ This is based on 3, 2 and 2 TDE candidates in samples of 550, > 2000 (Jones, Riess & Scolnic 2015), and \sim 2100 (Sako et al. 2014) Type Ia SNe.

Vanderbilt University, University of Virginia, University of Washington, and Yale University.

This publication makes use of data products from the Two Micron All Sky Survey, which is a joint project of the University of Massachusetts and the Infrared Processing and Analysis Center/California Institute of Technology, funded by the National Aeronautics and Space Administration and the National Science Foundation.

This publication makes use of data products from the Wide-field Infrared Survey Explorer, which is a joint project of the University of California, Los Angeles, and the Jet Propulsion Laboratory/California Institute of Technology, funded by the National Aeronautics and Space Administration.

This research has made use of the NASA/IPAC Extragalactic Database (NED), which is operated by the Jet Propulsion Laboratory, California Institute of Technology, under contract with the National Aeronautics and Space Administration.

REFERENCES

- Ahn C. P. et al., 2012, *ApJS*, 203, 21
 Arcavi I. et al., 2014, *ApJ*, 793, 38
 Assef R. J. et al., 2013, *ApJ*, 772, 26
 Barron J. T., Stumm C., Hogg D. W., Lang D., Roweis S., 2008, *AJ*, 135, 414
 Becker R. H., White R. L., Helfand D. J., 1995, *ApJ*, 450, 559
 Bloom J. S. et al., 2011, *Science*, 333, 203
 Botticella M. T. et al., 2010, *ApJL*, 717, L52
 Breeveld A. A. et al., 2010, *MNRAS*, 406, 1687
 Brown T. M. et al., 2013, *PASP*, 125, 1031
 Bruzual G., Charlot S., 2003, *MNRAS*, 344, 1000
 Burrows D. N. et al., 2005, *SSR*, 120, 165
 Burrows D. N. et al., 2011, *Nature*, 476, 421
 Cardelli J. A., Clayton G. C., Mathis J. S., 1988, *ApJL*, 329, L33
 Cenko S. B. et al., 2012a, *MNRAS*, 420, 2684
 Cenko S. B. et al., 2012b, *ApJ*, 753, 77
 Chornock R. et al., 2014, *ApJ*, 780, 44
 Denney K. D., Peterson B. M., Dietrich M., Vestergaard M., Bentz M. C., 2009, *ApJ*, 692, 246
 Donato D. et al., 2014, *ApJ*, 781, 59
 Dressler A. et al., 2011, *PASP*, 123, 288
 Evans C. R., Kochanek C. S., 1989, *ApJL*, 346, L13
 Fabricant D., Cheimets P., Caldwell N., Geary J., 1998, *PASP*, 110, 79
 Gezari S. et al., 2008, *ApJ*, 676, 944
 Gezari S. et al., 2012, *Nature*, 485, 217
 Gezari S. et al., 2009, *ApJ*, 698, 1367
 Goto T. et al., 2003, *PASJ*, 55, 771
 Graham A. W., Erwin P., Caon N., Trujillo I., 2001, *ApJL*, 563, L11
 Graham M. L. et al., 2014, *ApJ*, 787, 163
 Grupe D., Thomas H.-C., Leighly K. M., 1999, *AAP*, 350, L31
 Guillochon J., Manukian H., Ramirez-Ruiz E., 2014, *ApJ*, 783, 23
 Guillochon J., Ramirez-Ruiz E., 2015, preprint (arXiv:1501.05306)
 Hill J. E. et al., 2004, in *SPIE Conference Series*, Vol. 5165, X-Ray and Gamma-Ray Instrumentation for Astronomy XIII, Flanagan K. A., Siegmund O. H. W., eds., pp. 217–231
 Holoien T. W.-S. et al., 2014a, *MNRAS*, 445, 3263
 Holoien T. W.-S. et al., 2014b, preprint (arXiv:1411.3322)
 Holoien T. W.-S. et al., 2014c, *ApJL*, 785, L35
 Inserra C. et al., 2013, *ApJ*, 770, 128
 Jones D. O., Riess A. G., Scolnic D. M., 2015, *ArXiv e-prints*
 Jose J. et al., 2014, *The Astronomer’s Telegram*, 6777, 1
 Kalberla P. M. W., Burton W. B., Hartmann D., Arnal E. M., Bajaja E., Morras R., Pöppel W. G. L., 2005, *AAP*, 440, 775
 Kato T. et al., 2014, *PASJ*, 66, 90
 Kato T. et al., 2013, preprint (arXiv:1310.7069)
 Kochanek C. S., 1994, *ApJ*, 422, 508
 Komossa S., Greiner J., 1999, *AAP*, 349, L45
 Kriek M., van Dokkum P. G., Labbé I., Franx M., Illingworth G. D., Marchesini D., Quadri R. F., 2009, *ApJ*, 700, 221
 Lacy J. H., Townes C. H., Hollenbach D. J., 1982, *ApJ*, 262, 120
 Lantz B. et al., 2004, in *Society of Photo-Optical Instrumentation Engineers (SPIE) Conference Series*, Vol. 5249, Optical Design and Engineering, Mazuray L., Rogers P. J., Wartmann R., eds., pp. 146–155
 Levan A. J. et al., 2011, *Science*, 333, 199
 Li W. et al., 2011, *MNRAS*, 412, 1441
 Lodato G., Rossi E. M., 2011, *MNRAS*, 410, 359
 Loeb A., Ulmer A., 1997, *ApJ*, 489, 573
 Magorrian J., Tremaine S., 1999, *MNRAS*, 309, 447
 Martini P. et al., 2011, *PASP*, 123, 187
 McConnell N. J., Ma C.-P., 2013, *ApJ*, 764, 184
 Mendel J. T., Simard L., Palmer M., Ellison S. L., Patton D. R., 2014, *ApJS*, 210, 3
 Metzger B. D., Stone N. C., 2015, preprint (arXiv:1506.03453)
 Miller A. A. et al., 2009, *ApJ*, 690, 1303
 Peterson B. M. et al., 2004, *ApJ*, 613, 682
 Phinney E. S., 1989, *Nature*, 340, 595
 Pogge R. W. et al., 2010, in *Society of Photo-Optical Instrumentation Engineers (SPIE) Conference Series*, Vol. 7735, Society of Photo-Optical Instrumentation Engineers (SPIE) Conference Series
 Poole T. S. et al., 2008, *MNRAS*, 383, 627
 Rau A. et al., 2009, *PASP*, 121, 1334
 Rees M. J., 1988, *Nature*, 333, 523
 Roming P. W. A. et al., 2005, *SSR*, 120, 95
 Sako M. et al., 2014, preprint (arXiv:1401.3317)
 Schlafly E. F., Finkbeiner D. P., 2011, *ApJ*, 737, 103
 Schmidt S. J. et al., 2014, *ApJL*, 781, L24
 Shankar F., 2013, *Classical and Quantum Gravity*, 30, 244001
 Shappee B. J. et al., 2014, *ApJ*, 788, 48
 Shiokawa H., Krolik J. H., Cheng R. M., Piran T., Noble S. C., 2015, *ApJ*, 804, 85
 Skrutskie M. F. et al., 2006, *AJ*, 131, 1163
 Steele I. A. et al., 2004, in *Society of Photo-Optical Instrumentation Engineers (SPIE) Conference Series*, Vol. 5489, Ground-based Telescopes, Oschmann Jr. J. M., ed., pp. 679–692

- Stone N. C., Metzger B. D., 2014, preprint (arXiv:1410.7772)
Strubbe L. E., Quataert E., 2009, MNRAS, 400, 2070
Ulmer A., 1999, ApJ, 514, 180
van Velzen S., Farrar G. R., 2014, ApJ, 792, 53
van Velzen S. et al., 2011, ApJ, 741, 73
Voges W. et al., 1999, AAP, 349, 389
Wright E. L. et al., 2010, AJ, 140, 1868
Yun M. S., Reddy N. A., Condon J. J., 2001, ApJ, 554, 803
Zauderer B. A. et al., 2011, Nature, 476, 425

APPENDIX A: FOLLOW-UP PHOTOMETRY AND LINE LUMINOSITIES

All follow-up photometry and line luminosities are presented in Table A1 and Table A4 below, respectively. Photometry is presented in the natural system for each filter: *ugriz* magnitudes are in the AB system, while *Swift* filter magnitudes are in the Vega system.

Table A1. Photometric data of ASASSN-14li.

MJD	Magnitude	Filter	Telescope	MJD	Magnitude	Filter	Telescope
57007.258	15.013 0.013	<i>z</i>	LT	57017.529	15.284 0.012	<i>i</i>	LCOGT
57008.280	15.013 0.014	<i>z</i>	LT	57017.532	15.296 0.012	<i>i</i>	LCOGT
57009.275	15.102 0.013	<i>z</i>	LT	57018.163	15.265 0.010	<i>i</i>	LT
57011.227	15.087 0.014	<i>z</i>	LT	57019.155	15.270 0.009	<i>i</i>	LT
57012.211	15.028 0.014	<i>z</i>	LT	57020.319	15.284 0.013	<i>i</i>	LCOGT
57014.176	15.002 0.018	<i>z</i>	LT	57020.322	15.273 0.012	<i>i</i>	LCOGT
57016.213	15.027 0.013	<i>z</i>	LT	57021.155	15.274 0.009	<i>i</i>	LT
57017.205	15.120 0.014	<i>z</i>	LT	57021.701	15.316 0.012	<i>i</i>	LCOGT
57018.164	15.110 0.016	<i>z</i>	LT	57021.703	15.287 0.012	<i>i</i>	LCOGT
57019.156	15.095 0.015	<i>z</i>	LT	57024.214	15.302 0.010	<i>i</i>	LT
57020.153	15.038 0.022	<i>z</i>	LT	57025.277	15.286 0.008	<i>i</i>	LT
57021.156	15.076 0.014	<i>z</i>	LT	57025.692	15.287 0.018	<i>i</i>	LCOGT
57023.131	15.035 0.014	<i>z</i>	LT	57026.122	15.252 0.017	<i>i</i>	LT
57024.214	15.119 0.015	<i>z</i>	LT	57028.042	15.310 0.019	<i>i</i>	LCOGT
57025.277	15.114 0.011	<i>z</i>	LT	57029.145	15.286 0.013	<i>i</i>	LT
57026.122	15.033 0.018	<i>z</i>	LT	57029.679	15.296 0.002	<i>i</i>	LCOGT
57027.120	15.042 0.017	<i>z</i>	LT	57029.682	15.299 0.020	<i>i</i>	LCOGT
57028.200	15.110 0.013	<i>z</i>	LT	57032.031	15.288 0.024	<i>i</i>	LCOGT
57029.119	15.043 0.016	<i>z</i>	LT	57037.237	15.321 0.005	<i>i</i>	LT
57029.145	15.023 0.016	<i>z</i>	LT	57038.211	15.307 0.005	<i>i</i>	LT
57037.238	15.113 0.008	<i>z</i>	LT	57041.007	15.316 0.016	<i>i</i>	LCOGT
57038.212	15.115 0.007	<i>z</i>	LT	57041.010	15.319 0.016	<i>i</i>	LCOGT
57039.157	15.043 0.007	<i>z</i>	LT	57043.003	15.343 0.016	<i>i</i>	LCOGT
57041.138	15.056 0.008	<i>z</i>	LT	57043.006	15.329 0.016	<i>i</i>	LCOGT
57042.143	15.059 0.008	<i>z</i>	LT	57044.152	15.314 0.005	<i>i</i>	LT
57044.153	15.131 0.006	<i>z</i>	LT	57045.111	15.298 0.012	<i>i</i>	LCOGT
57046.083	15.149 0.007	<i>z</i>	LT	57045.113	15.321 0.012	<i>i</i>	LCOGT
57048.079	15.159 0.007	<i>z</i>	LT	57046.082	15.318 0.005	<i>i</i>	LT
57051.083	15.161 0.017	<i>z</i>	LT	57047.048	15.342 0.013	<i>i</i>	LCOGT
57053.056	15.142 0.008	<i>z</i>	LT	57047.050	15.303 0.013	<i>i</i>	LCOGT
57055.048	15.129 0.009	<i>z</i>	LT	57048.078	15.334 0.005	<i>i</i>	LT
57057.082	15.120 0.009	<i>z</i>	LT	57050.994	15.320 0.016	<i>i</i>	LCOGT
57059.043	15.157 0.010	<i>z</i>	LT	57051.082	15.356 0.016	<i>i</i>	LT
57065.160	15.135 0.007	<i>z</i>	LT	57053.054	15.321 0.006	<i>i</i>	LT
57068.143	15.136 0.007	<i>z</i>	LT	57055.047	15.311 0.007	<i>i</i>	LT
56989.467	15.291 0.053	<i>i</i>	LCOGT	57057.081	15.299 0.008	<i>i</i>	LT
57003.460	15.213 0.016	<i>i</i>	LCOGT	57059.042	15.276 0.009	<i>i</i>	LT
57003.462	15.178 0.015	<i>i</i>	LCOGT	57065.159	15.306 0.005	<i>i</i>	LT
57004.468	15.223 0.019	<i>i</i>	LCOGT	57068.142	15.316 0.005	<i>i</i>	LT
57004.471	15.253 0.019	<i>i</i>	LCOGT	56989.465	15.404 0.036	<i>r</i>	LT
57006.414	15.214 0.015	<i>i</i>	LCOGT	57007.257	15.375 0.008	<i>r</i>	LT
57006.417	15.203 0.016	<i>i</i>	LCOGT	57008.279	15.447 0.008	<i>r</i>	LT
57006.438	15.260 0.038	<i>i</i>	LCOGT	57009.274	15.453 0.007	<i>r</i>	LT
57006.441	15.234 0.033	<i>i</i>	LCOGT	57011.226	15.459 0.007	<i>r</i>	LT
57006.471	15.260 0.013	<i>i</i>	LCOGT	57012.210	15.396 0.007	<i>r</i>	LT
57006.473	15.279 0.013	<i>i</i>	LCOGT	57014.174	15.402 0.009	<i>r</i>	LT
57008.280	15.265 0.010	<i>i</i>	LT	57016.212	15.415 0.007	<i>r</i>	LT
57009.274	15.259 0.009	<i>i</i>	LT	57017.204	15.484 0.008	<i>r</i>	LT
57011.227	15.250 0.009	<i>i</i>	LT	57018.163	15.480 0.008	<i>r</i>	LT
57014.082	15.255 0.014	<i>i</i>	LCOGT	57019.155	15.461 0.008	<i>r</i>	LT
57014.089	15.233 0.015	<i>i</i>	LCOGT	57020.152	15.451 0.012	<i>r</i>	LT
57014.093	15.252 0.015	<i>i</i>	LCOGT	57021.154	15.485 0.008	<i>r</i>	LT
57016.076	15.298 0.012	<i>i</i>	LCOGT	57024.213	15.506 0.009	<i>r</i>	LT
57016.079	15.271 0.020	<i>i</i>	LCOGT	57025.276	15.503 0.008	<i>r</i>	LT
57017.205	15.277 0.009	<i>i</i>	LT	57026.121	15.503 0.019	<i>r</i>	LT

MJD	Magnitude	Filter	Telescope	MJD	Magnitude	Filter	Telescope		
57028.199	15.511	0.012	<i>r</i>	LT	57008.279	15.830	0.009	<i>g</i>	LT
57029.144	15.462	0.012	<i>r</i>	LT	57009.273	15.845	0.008	<i>g</i>	LT
57037.236	15.518	0.004	<i>r</i>	LT	57011.226	15.840	0.008	<i>g</i>	LT
57038.210	15.526	0.004	<i>r</i>	LT	57012.209	15.856	0.009	<i>g</i>	LT
57039.155	15.472	0.004	<i>r</i>	LT	57014.174	15.856	0.011	<i>g</i>	LT
57041.136	15.497	0.005	<i>r</i>	LT	57016.073	15.887	0.010	<i>g</i>	LCOGT
57042.141	15.493	0.004	<i>r</i>	LT	57016.211	15.857	0.008	<i>g</i>	LT
57044.151	15.535	0.004	<i>r</i>	LT	57017.203	15.887	0.008	<i>g</i>	LT
57046.081	15.539	0.004	<i>r</i>	LT	57017.526	15.910	0.008	<i>g</i>	LCOGT
57048.077	15.546	0.004	<i>r</i>	LT	57018.162	15.867	0.009	<i>g</i>	LT
57051.081	15.518	0.015	<i>r</i>	LT	57019.154	15.873	0.008	<i>g</i>	LT
57053.053	15.537	0.007	<i>r</i>	LT	57020.151	15.916	0.015	<i>g</i>	LT
57055.046	15.551	0.008	<i>r</i>	LT	57020.317	15.905	0.010	<i>g</i>	LCOGT
57057.080	15.558	0.009	<i>r</i>	LT	57021.154	15.900	0.008	<i>g</i>	LT
57059.041	15.550	0.011	<i>r</i>	LT	57021.698	15.931	0.011	<i>g</i>	LCOGT
57065.158	15.540	0.004	<i>r</i>	LT	57023.130	15.946	0.017	<i>g</i>	LT
57068.141	15.548	0.004	<i>r</i>	LT	57024.213	15.970	0.012	<i>g</i>	LT
56991.431	15.570	0.061	<i>V</i>	<i>Swift</i>	57025.275	15.930	0.008	<i>g</i>	LT
56993.888	15.670	0.061	<i>V</i>	<i>Swift</i>	57025.687	15.900	0.034	<i>g</i>	LCOGT
56995.292	15.570	0.061	<i>V</i>	<i>Swift</i>	57026.120	15.889	0.032	<i>g</i>	LT
56998.274	15.620	0.061	<i>V</i>	<i>Swift</i>	57027.118	15.942	0.024	<i>g</i>	LT
57001.608	15.470	0.051	<i>V</i>	<i>Swift</i>	57028.040	15.956	0.026	<i>g</i>	LCOGT
57004.264	15.700	0.100	<i>V</i>	<i>Swift</i>	57028.198	15.960	0.016	<i>g</i>	LT
57007.266	15.650	0.061	<i>V</i>	<i>Swift</i>	57029.117	15.948	0.021	<i>g</i>	LT
57010.803	15.630	0.061	<i>V</i>	<i>Swift</i>	57029.144	15.956	0.018	<i>g</i>	LT
57013.067	15.710	0.061	<i>V</i>	<i>Swift</i>	57029.677	15.958	0.030	<i>g</i>	LCOGT
57016.062	15.690	0.061	<i>V</i>	<i>Swift</i>	57037.235	15.963	0.004	<i>g</i>	LT
57019.515	15.720	0.071	<i>V</i>	<i>Swift</i>	57038.209	15.966	0.004	<i>g</i>	LT
57022.718	15.690	0.061	<i>V</i>	<i>Swift</i>	57039.154	15.968	0.004	<i>g</i>	LT
57029.319	15.690	0.081	<i>V</i>	<i>Swift</i>	57041.004	15.996	0.014	<i>g</i>	LCOGT
57033.113	15.780	0.081	<i>V</i>	<i>Swift</i>	57041.135	15.985	0.004	<i>g</i>	LT
57036.108	15.890	0.081	<i>V</i>	<i>Swift</i>	57042.140	15.975	0.004	<i>g</i>	LT
57039.036	15.870	0.071	<i>V</i>	<i>Swift</i>	57043.000	15.977	0.014	<i>g</i>	LCOGT
57042.230	15.940	0.091	<i>V</i>	<i>Swift</i>	57044.150	15.990	0.004	<i>g</i>	LT
57045.560	15.790	0.071	<i>V</i>	<i>Swift</i>	57045.108	15.986	0.010	<i>g</i>	LCOGT
57048.756	15.770	0.081	<i>V</i>	<i>Swift</i>	57046.080	15.993	0.004	<i>g</i>	LT
57051.468	15.750	0.081	<i>V</i>	<i>Swift</i>	57047.042	15.985	0.016	<i>g</i>	LCOGT
57054.007	15.750	0.081	<i>V</i>	<i>Swift</i>	57048.076	16.005	0.004	<i>g</i>	LT
57057.530	15.770	0.061	<i>V</i>	<i>Swift</i>	57051.080	15.974	0.020	<i>g</i>	LT
57059.798	15.830	0.091	<i>V</i>	<i>Swift</i>	57053.052	15.967	0.011	<i>g</i>	LT
57065.852	15.740	0.071	<i>V</i>	<i>Swift</i>	57055.045	16.036	0.013	<i>g</i>	LT
57068.781	15.810	0.061	<i>V</i>	<i>Swift</i>	57057.079	16.001	0.014	<i>g</i>	LT
57071.710	15.750	0.061	<i>V</i>	<i>Swift</i>	57059.040	16.073	0.017	<i>g</i>	LT
57074.848	15.800	0.081	<i>V</i>	<i>Swift</i>	57065.157	15.985	0.005	<i>g</i>	LT
57077.576	15.850	0.071	<i>V</i>	<i>Swift</i>	57068.130	16.006	0.003	<i>g</i>	LT
57080.891	15.700	0.110	<i>V</i>	<i>Swift</i>	57068.140	16.006	0.004	<i>g</i>	LT
57086.887	15.850	0.071	<i>V</i>	<i>Swift</i>	57070.125	16.021	0.003	<i>g</i>	LT
57089.350	15.760	0.061	<i>V</i>	<i>Swift</i>	57077.222	16.069	0.005	<i>g</i>	LT
57132.462	15.710	0.081	<i>V</i>	<i>Swift</i>	57079.071	16.062	0.003	<i>g</i>	LT
56989.463	15.752	0.041	<i>g</i>	LCOGT	57085.032	16.055	0.008	<i>g</i>	LT
57003.457	15.715	0.014	<i>g</i>	LCOGT	57093.076	16.082	0.004	<i>g</i>	LT
57004.465	15.740	0.016	<i>g</i>	LCOGT	57095.071	16.081	0.003	<i>g</i>	LT
57006.412	15.782	0.016	<i>g</i>	LCOGT	57097.994	16.095	0.003	<i>g</i>	LT
57006.436	15.797	0.056	<i>g</i>	LCOGT	57109.927	16.116	0.005	<i>g</i>	LT
57006.468	15.794	0.011	<i>g</i>	LCOGT	57112.017	16.112	0.009	<i>g</i>	LT
57007.256	15.798	0.010	<i>g</i>	LT	57113.968	16.102	0.011	<i>g</i>	LT

MJD	Magnitude	Filter	Telescope	MJD	Magnitude	Filter	Telescope
57117.977	16.110 0.009	<i>g</i>	LT	57020.153	16.716 0.134	<i>u</i>	LT
57121.021	16.099 0.004	<i>g</i>	LT	57021.156	16.744 0.090	<i>u</i>	LT
57122.959	16.115 0.003	<i>g</i>	LT	57024.215	16.842 0.069	<i>u</i>	LT
57124.975	16.114 0.003	<i>g</i>	LT	57025.278	16.842 0.052	<i>u</i>	LT
57127.004	16.114 0.003	<i>g</i>	LT	57029.146	16.844 0.125	<i>u</i>	LT
57129.961	16.106 0.003	<i>g</i>	LT	57037.239	16.976 0.033	<i>u</i>	LT
57132.982	16.128 0.003	<i>g</i>	LT	57038.213	17.054 0.030	<i>u</i>	LT
57135.962	16.125 0.003	<i>g</i>	LT	57039.158	17.050 0.033	<i>u</i>	LT
57138.944	16.111 0.004	<i>g</i>	LT	57041.139	16.970 0.044	<i>u</i>	LT
57142.113	16.152 0.008	<i>g</i>	LT	57042.144	17.070 0.037	<i>u</i>	LT
57147.941	16.117 0.005	<i>g</i>	LT	57044.154	17.036 0.030	<i>u</i>	LT
57150.951	16.127 0.003	<i>g</i>	LT	57046.084	17.024 0.049	<i>u</i>	LT
57153.912	16.127 0.004	<i>g</i>	LT	57048.080	17.034 0.045	<i>u</i>	LT
57158.925	16.105 0.004	<i>g</i>	LT	57051.084	16.995 0.117	<i>u</i>	LT
57161.893	16.110 0.003	<i>g</i>	LT	57053.057	17.106 0.077	<i>u</i>	LT
56991.426	15.960 0.045	<i>B</i>	<i>Swift</i>	57057.083	17.069 0.120	<i>u</i>	LT
56993.882	16.020 0.045	<i>B</i>	<i>Swift</i>	57059.044	16.981 0.223	<i>u</i>	LT
56995.275	15.930 0.045	<i>B</i>	<i>Swift</i>	57065.161	17.090 0.034	<i>u</i>	LT
56998.228	15.940 0.054	<i>B</i>	<i>Swift</i>	57068.132	17.126 0.014	<i>u</i>	LT
57001.602	16.010 0.045	<i>B</i>	<i>Swift</i>	57068.144	17.130 0.030	<i>u</i>	LT
57004.132	15.970 0.045	<i>B</i>	<i>Swift</i>	57070.128	17.126 0.015	<i>u</i>	LT
57007.260	16.050 0.045	<i>B</i>	<i>Swift</i>	57077.224	17.290 0.033	<i>u</i>	LT
57010.798	16.040 0.045	<i>B</i>	<i>Swift</i>	57079.073	17.258 0.017	<i>u</i>	LT
57013.061	16.060 0.045	<i>B</i>	<i>Swift</i>	57085.034	17.332 0.044	<i>u</i>	LT
57016.056	16.170 0.045	<i>B</i>	<i>Swift</i>	57093.078	17.370 0.019	<i>u</i>	LT
57019.510	16.160 0.054	<i>B</i>	<i>Swift</i>	57095.073	17.494 0.014	<i>u</i>	LT
57022.712	16.090 0.045	<i>B</i>	<i>Swift</i>	57097.996	17.518 0.015	<i>u</i>	LT
57029.315	16.180 0.063	<i>B</i>	<i>Swift</i>	57109.929	17.478 0.039	<i>u</i>	LT
57033.110	16.160 0.063	<i>B</i>	<i>Swift</i>	57112.019	17.391 0.045	<i>u</i>	LT
57036.045	16.310 0.063	<i>B</i>	<i>Swift</i>	57117.979	17.458 0.044	<i>u</i>	LT
57039.032	16.290 0.054	<i>B</i>	<i>Swift</i>	57121.023	17.526 0.022	<i>u</i>	LT
57042.228	16.180 0.063	<i>B</i>	<i>Swift</i>	57122.961	17.564 0.019	<i>u</i>	LT
57045.555	16.220 0.054	<i>B</i>	<i>Swift</i>	57124.977	17.510 0.017	<i>u</i>	LT
57048.752	16.300 0.054	<i>B</i>	<i>Swift</i>	57127.006	17.538 0.016	<i>u</i>	LT
57051.465	16.360 0.063	<i>B</i>	<i>Swift</i>	57129.963	17.540 0.017	<i>u</i>	LT
57054.004	16.260 0.063	<i>B</i>	<i>Swift</i>	57132.984	17.543 0.017	<i>u</i>	LT
57057.524	16.220 0.045	<i>B</i>	<i>Swift</i>	57135.965	17.524 0.017	<i>u</i>	LT
57059.796	16.310 0.063	<i>B</i>	<i>Swift</i>	57138.946	17.507 0.022	<i>u</i>	LT
57065.779	16.270 0.063	<i>B</i>	<i>Swift</i>	57142.115	17.484 0.040	<i>u</i>	LT
57068.775	16.270 0.045	<i>B</i>	<i>Swift</i>	57144.907	17.565 0.055	<i>u</i>	LT
57071.704	16.340 0.045	<i>B</i>	<i>Swift</i>	57150.953	17.543 0.017	<i>u</i>	LT
57074.844	16.270 0.054	<i>B</i>	<i>Swift</i>	57158.927	17.562 0.021	<i>u</i>	LT
57077.572	16.330 0.054	<i>B</i>	<i>Swift</i>	57161.895	17.572 0.018	<i>u</i>	LT
57080.889	16.340 0.082	<i>B</i>	<i>Swift</i>	56991.425	15.150 0.045	<i>U</i>	<i>Swift</i>
57086.882	16.340 0.054	<i>B</i>	<i>Swift</i>	56993.881	15.260 0.045	<i>U</i>	<i>Swift</i>
57089.344	16.340 0.045	<i>B</i>	<i>Swift</i>	56995.274	15.220 0.045	<i>U</i>	<i>Swift</i>
57132.459	16.390 0.063	<i>B</i>	<i>Swift</i>	56998.227	15.260 0.045	<i>U</i>	<i>Swift</i>
57007.258	16.586 0.059	<i>u</i>	LT	57001.601	15.280 0.045	<i>U</i>	<i>Swift</i>
57008.281	16.537 0.069	<i>u</i>	LT	57004.131	15.400 0.045	<i>U</i>	<i>Swift</i>
57009.276	16.585 0.062	<i>u</i>	LT	57007.259	15.470 0.045	<i>U</i>	<i>Swift</i>
57011.228	16.690 0.059	<i>u</i>	LT	57010.797	15.490 0.045	<i>U</i>	<i>Swift</i>
57012.212	16.724 0.062	<i>u</i>	LT	57013.060	15.420 0.045	<i>U</i>	<i>Swift</i>
57014.176	16.761 0.100	<i>u</i>	LT	57016.055	15.530 0.045	<i>U</i>	<i>Swift</i>
57016.214	16.749 0.060	<i>u</i>	LT	57019.510	15.600 0.054	<i>U</i>	<i>Swift</i>
57017.206	16.749 0.061	<i>u</i>	LT	57022.711	15.530 0.045	<i>U</i>	<i>Swift</i>
57018.164	16.784 0.077	<i>u</i>	LT	57029.315	15.750 0.063	<i>U</i>	<i>Swift</i>

MJD	Magnitude	Filter	Telescope	MJD	Magnitude	Filter	Telescope		
57033.109	15.800	0.063	<i>U</i>	<i>Swift</i>	57059.794	15.880	0.067	<i>W1</i>	<i>Swift</i>
57036.044	15.780	0.063	<i>U</i>	<i>Swift</i>	57065.776	15.920	0.058	<i>W1</i>	<i>Swift</i>
57039.031	15.860	0.063	<i>U</i>	<i>Swift</i>	57068.771	16.080	0.058	<i>W1</i>	<i>Swift</i>
57042.227	15.800	0.073	<i>U</i>	<i>Swift</i>	57071.700	15.930	0.050	<i>W1</i>	<i>Swift</i>
57045.555	15.880	0.063	<i>U</i>	<i>Swift</i>	57074.842	16.060	0.067	<i>W1</i>	<i>Swift</i>
57048.751	15.860	0.063	<i>U</i>	<i>Swift</i>	57077.569	16.160	0.067	<i>W1</i>	<i>Swift</i>
57051.464	15.870	0.063	<i>U</i>	<i>Swift</i>	57080.888	16.110	0.085	<i>W1</i>	<i>Swift</i>
57054.003	15.950	0.073	<i>U</i>	<i>Swift</i>	57086.878	16.250	0.058	<i>W1</i>	<i>Swift</i>
57057.523	15.940	0.054	<i>U</i>	<i>Swift</i>	57089.340	16.340	0.058	<i>W1</i>	<i>Swift</i>
57059.795	15.880	0.073	<i>U</i>	<i>Swift</i>	57099.391	16.450	0.067	<i>W1</i>	<i>Swift</i>
57065.778	15.960	0.073	<i>U</i>	<i>Swift</i>	57102.390	16.430	0.095	<i>W1</i>	<i>Swift</i>
57068.774	15.990	0.054	<i>U</i>	<i>Swift</i>	57105.254	16.700	0.143	<i>W1</i>	<i>Swift</i>
57071.703	15.950	0.054	<i>U</i>	<i>Swift</i>	57108.770	16.520	0.085	<i>W1</i>	<i>Swift</i>
57074.844	15.990	0.063	<i>U</i>	<i>Swift</i>	57111.899	16.500	0.058	<i>W1</i>	<i>Swift</i>
57077.571	16.030	0.063	<i>U</i>	<i>Swift</i>	57114.092	16.440	0.085	<i>W1</i>	<i>Swift</i>
57080.889	16.050	0.102	<i>U</i>	<i>Swift</i>	57117.688	16.470	0.058	<i>W1</i>	<i>Swift</i>
57086.881	16.170	0.063	<i>U</i>	<i>Swift</i>	57120.282	16.620	0.067	<i>W1</i>	<i>Swift</i>
57089.343	16.230	0.063	<i>U</i>	<i>Swift</i>	57123.544	16.640	0.067	<i>W1</i>	<i>Swift</i>
57099.394	16.190	0.054	<i>U</i>	<i>Swift</i>	57126.136	16.740	0.085	<i>W1</i>	<i>Swift</i>
57102.391	16.170	0.082	<i>U</i>	<i>Swift</i>	57129.201	16.880	0.085	<i>W1</i>	<i>Swift</i>
57108.771	16.270	0.073	<i>U</i>	<i>Swift</i>	57132.457	16.650	0.085	<i>W1</i>	<i>Swift</i>
57111.902	16.280	0.054	<i>U</i>	<i>Swift</i>	57136.118	16.680	0.095	<i>W1</i>	<i>Swift</i>
57114.093	16.330	0.073	<i>U</i>	<i>Swift</i>	57139.314	16.740	0.067	<i>W1</i>	<i>Swift</i>
57117.692	16.350	0.054	<i>U</i>	<i>Swift</i>	57147.562	16.750	0.067	<i>W1</i>	<i>Swift</i>
57120.285	16.340	0.054	<i>U</i>	<i>Swift</i>	57150.224	16.770	0.058	<i>W1</i>	<i>Swift</i>
57123.547	16.380	0.054	<i>U</i>	<i>Swift</i>	57153.418	16.730	0.067	<i>W1</i>	<i>Swift</i>
57126.138	16.430	0.073	<i>U</i>	<i>Swift</i>	57156.350	16.740	0.114	<i>W1</i>	<i>Swift</i>
57129.202	16.400	0.073	<i>U</i>	<i>Swift</i>	56991.432	14.460	0.042	<i>M2</i>	<i>Swift</i>
57132.458	16.530	0.092	<i>U</i>	<i>Swift</i>	56993.889	14.910	0.042	<i>M2</i>	<i>Swift</i>
57136.119	16.470	0.082	<i>U</i>	<i>Swift</i>	56995.283	14.540	0.042	<i>M2</i>	<i>Swift</i>
57139.317	16.450	0.054	<i>U</i>	<i>Swift</i>	56998.275	14.680	0.036	<i>M2</i>	<i>Swift</i>
57147.565	16.480	0.054	<i>U</i>	<i>Swift</i>	57001.609	14.680	0.042	<i>M2</i>	<i>Swift</i>
57150.228	16.340	0.045	<i>U</i>	<i>Swift</i>	57004.264	14.730	0.050	<i>M2</i>	<i>Swift</i>
57153.420	16.450	0.063	<i>U</i>	<i>Swift</i>	57007.268	14.900	0.042	<i>M2</i>	<i>Swift</i>
57156.351	16.540	0.102	<i>U</i>	<i>Swift</i>	57010.804	14.940	0.042	<i>M2</i>	<i>Swift</i>
56991.423	14.730	0.042	<i>W1</i>	<i>Swift</i>	57013.068	14.950	0.042	<i>M2</i>	<i>Swift</i>
56993.878	14.980	0.042	<i>W1</i>	<i>Swift</i>	57016.063	15.140	0.042	<i>M2</i>	<i>Swift</i>
56995.271	14.820	0.042	<i>W1</i>	<i>Swift</i>	57019.516	15.170	0.042	<i>M2</i>	<i>Swift</i>
56998.225	14.880	0.050	<i>W1</i>	<i>Swift</i>	57022.719	15.180	0.042	<i>M2</i>	<i>Swift</i>
57001.598	14.890	0.042	<i>W1</i>	<i>Swift</i>	57029.319	15.580	0.050	<i>M2</i>	<i>Swift</i>
57004.128	14.940	0.042	<i>W1</i>	<i>Swift</i>	57033.114	15.370	0.050	<i>M2</i>	<i>Swift</i>
57007.256	15.150	0.042	<i>W1</i>	<i>Swift</i>	57036.109	15.490	0.050	<i>M2</i>	<i>Swift</i>
57010.794	15.240	0.042	<i>W1</i>	<i>Swift</i>	57039.037	15.500	0.050	<i>M2</i>	<i>Swift</i>
57013.057	15.210	0.042	<i>W1</i>	<i>Swift</i>	57042.231	15.620	0.058	<i>M2</i>	<i>Swift</i>
57016.052	15.340	0.050	<i>W1</i>	<i>Swift</i>	57045.561	15.620	0.050	<i>M2</i>	<i>Swift</i>
57019.507	15.400	0.050	<i>W1</i>	<i>Swift</i>	57051.469	15.660	0.050	<i>M2</i>	<i>Swift</i>
57022.708	15.390	0.050	<i>W1</i>	<i>Swift</i>	57054.007	15.670	0.050	<i>M2</i>	<i>Swift</i>
57029.313	15.620	0.058	<i>W1</i>	<i>Swift</i>	57057.531	15.740	0.050	<i>M2</i>	<i>Swift</i>
57033.038	15.690	0.058	<i>W1</i>	<i>Swift</i>	57059.799	15.780	0.058	<i>M2</i>	<i>Swift</i>
57036.042	15.640	0.050	<i>W1</i>	<i>Swift</i>	57065.853	15.700	0.076	<i>M2</i>	<i>Swift</i>
57039.029	15.730	0.050	<i>W1</i>	<i>Swift</i>	57068.782	16.070	0.050	<i>M2</i>	<i>Swift</i>
57042.226	15.750	0.067	<i>W1</i>	<i>Swift</i>	57071.711	15.870	0.050	<i>M2</i>	<i>Swift</i>
57045.552	15.820	0.058	<i>W1</i>	<i>Swift</i>	57074.848	15.950	0.058	<i>M2</i>	<i>Swift</i>
57051.463	15.780	0.058	<i>W1</i>	<i>Swift</i>	57077.577	16.020	0.050	<i>M2</i>	<i>Swift</i>
57054.002	15.780	0.067	<i>W1</i>	<i>Swift</i>	57080.891	16.120	0.076	<i>M2</i>	<i>Swift</i>
57057.520	15.770	0.050	<i>W1</i>	<i>Swift</i>	57086.888	16.130	0.050	<i>M2</i>	<i>Swift</i>

MJD	Magnitude	Filter	Telescope	MJD	Magnitude	Filter	Telescope
57089.351	16.300 0.050	M2	<i>Swift</i>	57036.046	15.560 0.058	W2	<i>Swift</i>
57099.388	16.310 0.067	M2	<i>Swift</i>	57039.033	15.350 0.042	W2	<i>Swift</i>
57102.389	16.600 0.104	M2	<i>Swift</i>	57042.228	15.400 0.050	W2	<i>Swift</i>
57105.250	16.450 0.058	M2	<i>Swift</i>	57045.556	15.510 0.050	W2	<i>Swift</i>
57108.768	16.490 0.085	M2	<i>Swift</i>	57051.466	15.440 0.050	W2	<i>Swift</i>
57111.895	16.580 0.067	M2	<i>Swift</i>	57054.004	15.550 0.050	W2	<i>Swift</i>
57114.090	16.570 0.095	M2	<i>Swift</i>	57057.525	15.570 0.042	W2	<i>Swift</i>
57117.683	16.560 0.058	M2	<i>Swift</i>	57059.796	15.580 0.050	W2	<i>Swift</i>
57120.278	16.700 0.067	M2	<i>Swift</i>	57065.779	15.550 0.085	W2	<i>Swift</i>
57123.540	16.670 0.067	M2	<i>Swift</i>	57068.776	16.050 0.050	W2	<i>Swift</i>
57126.134	16.770 0.085	M2	<i>Swift</i>	57071.705	15.740 0.042	W2	<i>Swift</i>
57129.198	16.810 0.085	M2	<i>Swift</i>	57074.845	15.770 0.050	W2	<i>Swift</i>
57132.462	16.740 0.076	M2	<i>Swift</i>	57077.573	15.800 0.050	W2	<i>Swift</i>
57136.116	16.790 0.104	M2	<i>Swift</i>	57080.890	15.940 0.067	W2	<i>Swift</i>
57139.309	16.670 0.067	M2	<i>Swift</i>	57086.883	16.030 0.050	W2	<i>Swift</i>
57147.558	16.790 0.067	M2	<i>Swift</i>	57089.345	16.120 0.050	W2	<i>Swift</i>
57150.218	16.850 0.067	M2	<i>Swift</i>	57099.395	16.250 0.050	W2	<i>Swift</i>
57153.414	16.750 0.076	M2	<i>Swift</i>	57102.392	16.360 0.067	W2	<i>Swift</i>
57156.349	16.860 0.124	M2	<i>Swift</i>	57108.772	16.310 0.067	W2	<i>Swift</i>
56991.427	14.260 0.042	W2	<i>Swift</i>	57111.904	16.450 0.050	W2	<i>Swift</i>
56993.883	14.700 0.042	W2	<i>Swift</i>	57114.094	16.350 0.067	W2	<i>Swift</i>
56995.276	14.310 0.042	W2	<i>Swift</i>	57117.694	16.480 0.058	W2	<i>Swift</i>
56998.229	14.360 0.050	W2	<i>Swift</i>	57120.286	16.690 0.058	W2	<i>Swift</i>
57001.603	14.460 0.042	W2	<i>Swift</i>	57123.549	16.630 0.058	W2	<i>Swift</i>
57004.133	14.480 0.042	W2	<i>Swift</i>	57126.139	16.760 0.067	W2	<i>Swift</i>
57007.261	14.690 0.042	W2	<i>Swift</i>	57129.203	16.830 0.076	W2	<i>Swift</i>
57010.799	14.770 0.042	W2	<i>Swift</i>	57132.459	16.660 0.067	W2	<i>Swift</i>
57013.062	14.730 0.042	W2	<i>Swift</i>	57136.120	16.660 0.076	W2	<i>Swift</i>
57016.057	14.920 0.042	W2	<i>Swift</i>	57139.318	16.590 0.050	W2	<i>Swift</i>
57019.511	15.010 0.042	W2	<i>Swift</i>	57147.567	16.670 0.050	W2	<i>Swift</i>
57022.713	14.990 0.042	W2	<i>Swift</i>	57150.230	16.720 0.050	W2	<i>Swift</i>
57029.316	15.380 0.050	W2	<i>Swift</i>	57153.422	16.790 0.058	W2	<i>Swift</i>
57033.111	15.170 0.050	W2	<i>Swift</i>	57156.352	16.680 0.085	W2	<i>Swift</i>

Magnitudes and uncertainties are presented in the natural system for each filter: *ugriz* magnitudes are presented in the AB system, *Swift* filter magnitudes are presented in the Vega system. Uncertainties are given next to the magnitude measurements. Data are not corrected for Galactic extinction.

Table A2. Swift XRT photometry of ASASSN-14li.

MJD	Flux	Uncertainty	Count Rate	Uncertainty	MJD	Flux	Uncertainty	Count Rate	Uncertainty
56991.5	1.81	0.10	0.35	0.01	57068.5	1.60	0.12	0.24	0.01
56993.5	1.89	0.10	0.33	0.01	57071.5	1.64	0.10	0.25	0.01
56995.5	2.09	0.09	0.33	0.01	57074.5	1.68	0.10	0.24	0.01
56998.5	1.92	0.10	0.41	0.02	57077.5	1.56	0.15	0.19	0.01
57001.5	2.01	0.09	0.39	0.02	57080.5	1.85	0.10	0.24	0.01
57004.5	2.17	0.18	0.41	0.02	57086.9	1.81	0.10	0.27	0.01
57007.5	2.60	0.09	0.45	0.02	57089.3	1.58	0.08	0.30	0.01
57010.5	2.60	0.11	0.48	0.02	57099.4	2.11	0.17	0.25	0.01
57013.5	2.27	0.09	0.43	0.02	57102.6	1.71	0.10	0.23	0.01
57016.5	1.98	0.09	0.45	0.02	57109.2	1.77	0.12	0.23	0.01
57019.5	2.17	0.07	0.40	0.01	57111.9	2.34	0.11	0.23	0.01
57022.5	2.36	0.11	0.33	0.01	57114.1	1.48	0.10	0.20	0.01
57029.5	2.22	0.07	0.40	0.01	57117.7	2.03	0.13	0.20	0.01
57033.5	2.29	0.11	0.36	0.02	57120.3	1.51	0.08	0.19	0.01
57037.5	2.50	0.11	0.39	0.02	57123.6	1.70	0.13	0.19	0.01
57040.5	2.01	0.12	0.35	0.01	57126.2	1.53	0.10	0.17	0.01
57043.5	1.89	0.09	0.36	0.02	57129.4	1.62	0.13	0.18	0.01
57046.5	1.99	0.11	0.36	0.02	57132.6	1.08	0.09	0.16	0.01
57048.5	1.91	0.09	0.33	0.01	57136.6	1.05	0.07	0.15	0.01
57051.5	2.00	0.09	0.30	0.02	57139.3	1.38	0.13	0.17	0.01
57053.5	1.77	0.09	0.31	0.01	57147.6	1.05	0.08	0.14	0.01
57057.5	1.80	0.09	0.28	0.01	57150.3	1.72	0.14	0.15	0.01
57059.5	1.65	0.08	0.29	0.01	57153.5	1.39	0.10	0.15	0.01
57065.5	1.66	0.10	0.20	0.01	57156.7	1.18	0.11	0.15	0.01

All X-ray fluxes and flux uncertainties are given in units of 10^{-11} ergs s^{-1} cm^{-2} while count rates and count rate uncertainties are given in counts s^{-1} . The Swift XRT energy range is 0.3 – 10 keV. Data are not corrected for Galactic extinction.

Table A3. Spectroscopic Observations of ASASSN-14li.

UT Date	MJD	Telescope/Instrument	Exposure (s)
2014 November 30.60	56991.60	UH-2.2m/SNIFS	2×400
2014 December 02.51	56993.51	APO-3.5m/DIS	2×1000
2014 December 09.51	57000.51	MDM-2.4m/Modspec	4×600
2014 December 10.56	57001.56	MDM-2.4m/Modspec	3×240
2014 December 12.48	57003.48	APO-3.5m/DIS	2×1200
2014 December 12.54	57003.54	MDM-2.4m/Modspec	1×600
2014 December 14.49	57005.49	FLWO-1.5m/FAST	3×900
2014 December 15.51	57006.51	FLWO-1.5m/FAST	3×1200
2014 December 19.49	57010.49	FLWO-1.5m/FAST	1×1800
2014 December 23.51	57014.51	MDM-2.4m/OSMOS	3×1200
2015 January 03.35	57025.35	Magellan-6.5m/IMACS	2×500
2015 January 20.53	57042.53	LBT-8.4m/MODS	2×900
2015 February 11.40	57064.40	MDM-2.4m/OSMOS	3×1200
2015 February 14.50	57067.50	FLWO-1.5m/FAST	2×1200
2015 February 15.38	57069.38	LBT-8.4m/MODS	3×1200
2015 March 11.35	57092.35	MDM-2.4m/OSMOS	3×1200
2015 April 17.19	57129.19	LBT-8.4m/MODS	3×900

Table A4. Line luminosities for ASASSN-14li.

MJD	H α (6563 Å)	H β (4861 Å)	He II (4686 Å)
56993.51	1.01×10^{41}	3.85×10^{40}	5.07×10^{40}
57001.56	1.01×10^{41}	2.98×10^{40}	5.53×10^{40}
57003.48	1.12×10^{41}	3.65×10^{40}	7.09×10^{40}
57003.54	8.27×10^{40}	2.80×10^{40}	5.45×10^{40}
57005.49	9.72×10^{40}	3.65×10^{40}	6.06×10^{40}
57006.51	7.69×10^{40}	5.63×10^{40}	8.67×10^{40}
57010.49	9.86×10^{40}	2.82×10^{40}	6.52×10^{40}
57014.51	6.72×10^{40}	2.64×10^{40}	3.12×10^{40}
57025.35	6.58×10^{40}	1.99×10^{40}	3.77×10^{40}
57042.53	4.90×10^{40}	1.91×10^{40}	5.07×10^{40}
57064.40	2.10×10^{40}	1.29×10^{40}	3.79×10^{40}
57067.49	2.55×10^{40}	1.42×10^{40}	2.38×10^{40}
57069.38	4.07×10^{40}	1.16×10^{40}	2.91×10^{40}
57092.35	1.41×10^{40}	—	2.05×10^{40}
57129.19	1.59×10^{40}	6.96×10^{39}	1.70×10^{40}

Column headers indicate the lines used to measure the luminosities. All luminosities are given in units of ergs s^{-1} . No value is given for epochs where a measurement was not possible.